Ultrafast Electron Diffraction Studies of Optically Excited Thin Bismuth Films

Vom Fachbereich Physik der Universität Duisburg-Essen zur Erlangung des akademischen Grades eines Doktors der Naturwissenschaften genehmigte

Dissertation

von

Ivan Rajkovic

aus

Aleksinac

Referent: Prof. Dr. Dietrich von der Linde

Korreferent: Prof. Dr. Michael Horn-von Hoegen

Tag der mündlichen Prüfung: 21.10.2008

Acknowledgements

I would like to thank my supervisor, Prof. Dr. Dietrich von der Linde, for providing me with the opportunity to do my PhD thesis research in his group at the Institut für Experimentelle Physik at the University of Duisburg-Essen and for his support and guidance during my work there.

I would also like to give special thanks to the people I worked with on this project, Ping Zhou and Manuel Ligges. Without them, this work would not be possible.

Then, I would like to thank Nikola Stojanović for all of his help, both in and out of the lab.

Many thanks go to all of the people working in the AG von der Linde: Dr. Klaus Sokolowski-Tinten, Dr. Alexander Tarasevitch, Matthieu Nicoul, Dr. Uladzimir Shymanovich, Stephan Kähle, Dr. Oliver Heinz, Dr. Vasily Temnov, Wei Lu, Jan Göhre, Konstantin Lobov, Barbel Maüllu, Dr. Ulrich Teubner and all of the diploma students and the student assistants who contributed to the wonderful working atmosphere in this group.

A special thanks to Mrs. Kay Eibl, the group secretary, who was always extremely helpfull with our various paperwork and who helped me improve English language in this thesis.

I would like to thank our technical staff, Michael Bieske, Bernd Proff and Doris Steeger, for solving many mechanical and electrical problems.

I would also like to thank Thomas Payer and Dr. Frank Meyer zu Heringdorf for growing bismuth samples for the experiments.

Finally, I would like to thank Prof. Dr. Dietrich von der Linde, Prof. Dr. Michael Horn-von Hoegen and Prof. Dr. Lothar Schäfer for being members of the examination board for my thesis.

Contents

1 Introduction **1**

1.1 The beginning of time-resolved experiments 1

1.2 Watching structure change 4

1.3 Thesis overview 8

2 Electron pulses **9**

2.1 Acceleration region 11

2.2 Drift region 13

2.2.1 Mean field model 13

2.3 Divergence of electron pulses 17

2.4 Focusing of electron pulses 19

2.4.1 Electrostatic lens 20

2.4.2 Magnetic lens 22

3 Characterization of the electron source **27**

3.1 Experimental Setup 28

3.1.1 Electron source 28

3.1.2 Laser system 31

3.2 Experimental setup 34
3.3 Focusing of electron pulses 35
3.3.1 Focusing with an electrostatic lens 35
3.3.2 Focusing with a magnetic lens 37
3.4 Determining the number of electrons per pulse 42

4 Theoretical introduction to the electron diffraction 47
4.1 Bragg's law 47
4.2 Ewald sphere 50
4.3 Effect of a thin film 50
4.4 Structure factors 52
4.5 Debye-Waller effect 53

5 Time resolved experiments 57
5.1 Experimental setup 57
5.2 Spatial overlap between the laser beam and the electron probe beam 60
5.3 Temporal overlap between the laser pump and the electron probe beams 61
5.4 Temporal resolution 65
5.5 Sample preparation 67
5.6 Stability of the electron source 69
5.6.1 Short-term stability 70
5.6.2 Long-term stability 75
5.7 Time resolved measurements 76

6 Results and Discussion **81**

6.1 Data analysis 81

6.1.1 Non-diffracted beam 90

7 Summary and conclusion **93**

A Leapfrog integration **97**

A.1 Matlab code for leapfrog integration 98

B Bismuth properties **101**

Chapter 1

Introduction

Since the beginning of human kind, people have always wanted to find the answer to the question *why* certain things are happening. The insecurity of not knowing by which laws nature is behaving has caused them to seek and find answers to this oldest of questions. Once they discovered *why* system *S* changed its state from *A* to *B*, some new question arose. Among these subsequent questions was ***HOW***. It was not enough just to know the starting and the ending state, it was important to know all the steps that the system went through. The answer to this question, *how*, is provided by time-resolved experiments.

1.1 The beginning of time-resolved experiments

The history of time-resolved experiments began with the development of high speed photography, in the second half of the 19^{th} century. At this time, the first pictures with an exposition time of $\sim$1 ms were made.

The first known time-resolved measurement using high speed cameras was made in 1878, in Palo Alto, USA. It was performed by Eadweard Muybridge who was hired by Leland Stanford to prove that at some point in time during the trot gait, a horse has all four legs off the ground simultaneously. This was accomplished by using a set of 24 cameras and specially developed shutters which gave an exposure time of 2 ms. The resulting photos can be seen in Fig 1.1.

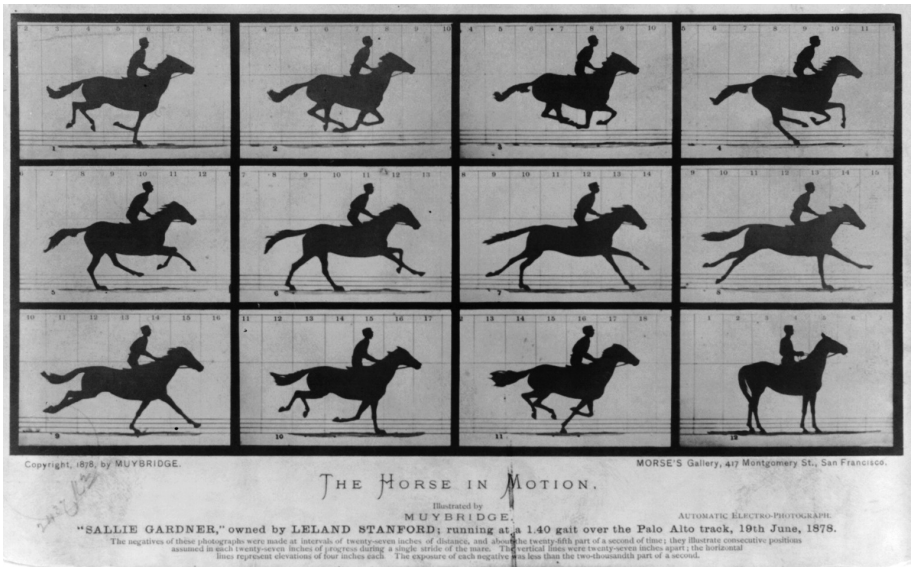

Figure 1.1: First time-resolved measurement: The Horse in Motion. Image taken from Library of Congress Prints and Photographs Division Washington, D.C. 20540 USA

A few years later, in 1882, Étienne-Jules Marey, a professor at the College de France, used a photographic gun camera, which could take 12 pictures per second with an exposition of 1/720 s, to record the movements of birds. One of his photos can be seen in Fig 1.2.

Between 1880 and 1930, various high speed photographic systems were developed all over the world. In the 1930s, Dr. Harold Edgerton developed the Stroboscopic Flash System, which provided extremely short duration light

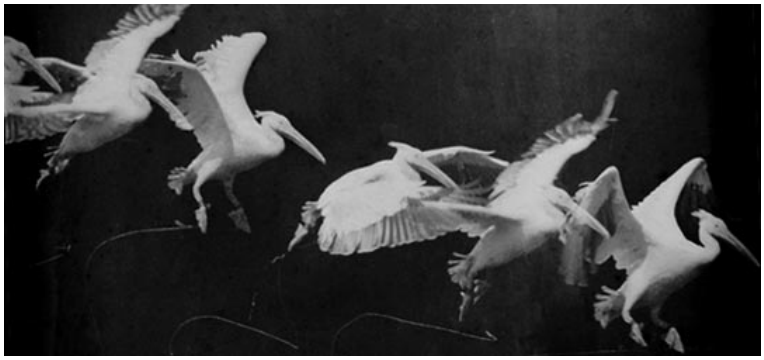

Figure 1.2: Time resolved movements of the pelican. Photo was taken by Étienne-Jules Marey in 1882.

sources to 'freeze' action and allow a detailed look at sequential events. One of his first photographs is shown in Figure 1.3, a stream of water coming out of a faucet.

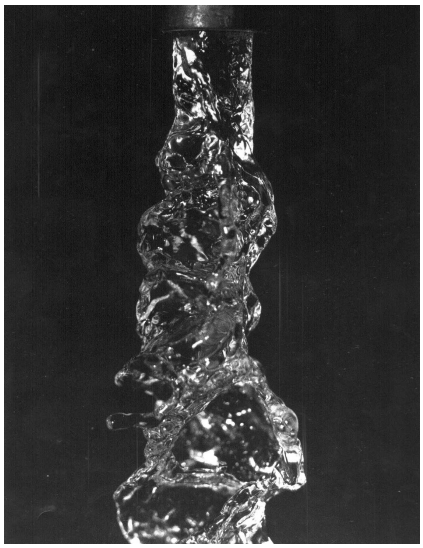

Figure 1.3: A stream of water coming out of a faucet. Photo was taken by Dr. Harold Edgerton.

This was the birth of the pump-probe experiment. The resolution of the time-

resolved experiment no longer depended on the speed of the mechanical shutter, but on the duration of the probe pulse.

With the discovery of the laser, it was possible to further reduce the duration of the probe pulse. In 1961, Q-switching made it possible to achieve resolution of a few tens of ns. A couple of years later, in 1963, using mode locking, the duration of laser pulses came into a ps range. The problem was that these short pulses, when amplified to the intensities larger than several GW/cm^2, could suffer from excessive nonlinear pulse distortions or thermally damage the gain medium. This problem was solved in 1985, with the invention of the CPA (Chirped Pulse Amplification) [Ref. 1, 2].

1.2 Watching structure change

When an ultrashort laser pulse is absorbed in some material, the energy of the pulse is first transfered to the electrons, while the lattice remains cold. The transfer of energy from the excited electrons to the lattice can occur on a time scale of femtoseconds to picoseconds, depending on the strength of electron-phonon coupling.

In order to directly observe changes in an atomic structure with the atomic resolution ($\sim$Å), ultrashort radiation with wavelengths comparable to the crystal lattice parameters or to the molecular bond length should be used. Since these lengths are in the order of a few angstroms, the first choice was to use X-rays as the probe beam and to look at the diffraction pattern.

The first sub-picosecond X-ray sources were developed in the late '80s/early

'90s, and were plasma based [Ref. 3, 4]. The first sub-ps time resolved experiment using X-rays as a probe was performed in 1997 [Ref. 5]. Also, in the following years, the accelerator based X-rays sources were used for generating sub-ps X-rays pulses [Ref. 6, 7].

Although X-rays have been proven to be adequate for observing structural changes in time-resolved experiments, they do have some disadvantages. First, by using a monoenergetic laser-plasma X-ray beam, it is normally possible to fulfill Bragg's condition for only one diffraction peak. In order to observe another peak, the sample has to be rotated to the position for which Bragg's condition is fulfilled for a specific diffraction order. Also, the X-rays penetrate deep into a material, in the range of a μm, while the material is optically excited usually only up to a few $\sim$100nm, as determined by the penetration depth of the pump beam. This can be solved by using small incident angles for X-rays ('grazing incident') or by preparing the samples in a special way, for example, a thin sample on a substrate with different lattice constants.

An an alternative choice for a probe beam, electrons can be used instead of X-rays. The first ultrafast electron diffraction setup with sub-ps time resolution used 30keV electrons as a probe beam (Siwick et al., [Ref. 8, 9]).

The most important advantage of these electrons is that they have much larger (10^5-10^6 times) scattering cross-section than X-rays. Due to the large scattering cross-section, the penetration depth is smaller, so it is possible to probe just the volume excited by the laser pulse and get an intense diffracted signal. Furthermore, due to the small de Broglie wavelength of these electrons (0.07 Å for 30 keV electrons), the Bragg's condition is fulfilled for various reciprocal

lattice vectors, so that multiple diffraction orders can be observed at the same time. This way, it is possible to simultaneously obtain much more information - 'All at once' [Ref. 10].

The shortcomings of using the electrons as a probe beam are:

1) They interact with each other via the Coulomb force, so that the electrons at the front and the back of the pulse get pushed further away from the center of the pulse. This results in the temporal broadening of the pulses.

2) They have a velocity distribution, which also temporally broadens the pulses.

These effects will be discussed in detail in Chapter 2. The challenge of time resolved ultrafast electron diffraction experiments is to minimize the effects that temporally broaden electron pulses in order to achieve an electron pulse duration of less than one picosecond.

The first use of electron diffraction with picosecond pulses had a temporal resolution of 20-100 ps, and only one diffraction ring could be observed [Ref. 11]. In the first ultrafast electron diffraction experiment with sub-picosecond resolution [Ref. 9], the melting of aluminium was measured. Similar experiments were performed with silver, where the shift of the Bragg peaks was observed [Ref. 12]. In other experiments, the coherent and random motion of the lattice was measured in aluminium, and the optical control of the coherent lattice motion was demonstrated [Ref. 13, 14]. Both the destructive and the non-destructive measurements were done on silicon [Ref. 15, 16], showing the structure changes and the lattice heating dynamics.

Using the molecular beam as a sample, it was possible to observe the dynamics of the chemical reactions of molecules, e.g. for aromatic carbonyls, ace-

tophenone and benzaldehyde [Ref. 17, 18] and for vanadium dioxide [Ref. 19]. To be able to see breaking and forming of molecular bonds, to directly observe molecular transition states was one of the most important questions for chemistry, referred to as one of the 'Holy Grails' for the field [Ref. 20].

Due to the short penetration depth, electron diffraction is an excellent choice for surface science time-resolved experiments. Two different types of experiments can be made: low-energy electron diffraction (LEED) and reflective high-energy electron diffraction (RHEED). LEED uses electrons with energies in a range from a few tens to a few hundreds of eV which are elastically backscattered for the sample. With these electron energies, it is very difficult to achieve short electron pulses and have high temporal resolution [Ref. 21]. For RHEED, electrons with higher energies are used, in a range of a few tens of keV. Since the diffraction angles for these electrons are relatively small, it is necessary for electrons to probe a surface with a small incoming angle. Due to the velocity mismatch between the laser pump and the electron probe pulses, the temporal resolution of these experiments is limited to several tens of picoseconds [Ref. 22–25].

When using an optical grating to tilt a pump pulse front [Ref. 26, 27], it was possible to compensate for the small incoming angle of the electron probe pulse and the velocity mismatch so that, at every point at the sample surface, a time-delay between the pump and the probe pulse was the same. In this way a picosecond time resolution was achieved in surface measurements [Ref. 28, 29].

Recently, there have been a few theoretical works showing that it should be possible to compress electron pulses to a 30 fs duration using a RF cavity [Ref. 30, 31]. Once experimentally realized, this would greatly improve the

time resolution of ultrafast electron diffraction experiments. Also, it has been proposed to use a tilted pulse front for producing electrons and then use an acceleration element with a linear voltage gradient. This would lead to autocompressing of the pulses [Ref. 28] and would make it possible to obtain sub-picosecond electron pulses with a higher number of electrons.

1.3 Thesis overview

The goal of this thesis is the development of an experimental setup capable of performing ultrafast electron diffraction experiments with a time resolution better than 1 ps.

In Chapter 2, the propagation dynamics of the electron pulses will be discussed. Here it will be explained how the duration of the electron pulses increases during their propagation and how to keep this increase minimal.

In Chapter 3, the experimental setup built for obtaining sub-ps electron pulses will be presented and the electron source will be characterized. Also, the electron optics needed for focusing the electron beam will be explained.

In Chapter 4, the diffraction theory will be briefly discussed.

Chapter 5 will focus on time-resolved pump-probe experiments with bismuth, while in Chapter 6 the results of these experiments will be presented and discussed.

Finally, in Chapter 7, there will be a summary of this thesis and an outlook with regards to future experiments will be presented.

Chapter 2

Electron pulses

In order to produce electron pulses with sub-picosecond duration, the reasons for their temporal broadening have to be understood. The dynamics of the electron pulses will be discussed in this chapter.

Using the ultrashort Ti:Sapphire laser pulses, it is possible to produce electron bunches with a duration comparable to the laser pulse duration, less than 100 fs. However, these electron bunches experience temporal broadening, which is one of the biggest problems in achieving sub-picosecond temporal resolution in the electron diffraction measurements. There are two main reasons for the temporal broadening: the repulsion of the electrons due to the Coulomb force (the space-charge effect) and the initial kinetic energy distribution of the electron pulse.

Figure 2.1 shows a schematic of the electron source. It consists of a back-illuminated photocathode and an anode with a pinhole. The photocathode is kept on a negative potential, while the anode is grounded. The UV laser beam hits

the photocathode and extracts electrons which are then accelerated in the high electric field between the electrodes. After passing through the pinhole in the anode, the electrons are sent to the sample.

The pulse broadening in two regions of the electron source (see Fig. 2.1) will be explained in the next 2 sections. The first region is between the photocathode and the pinhole, where electrons are accelerated *(a)*. The second is between the pinhole and the sample, where electron pulses are traveling with the constant velocity - drifting region *(b)*.

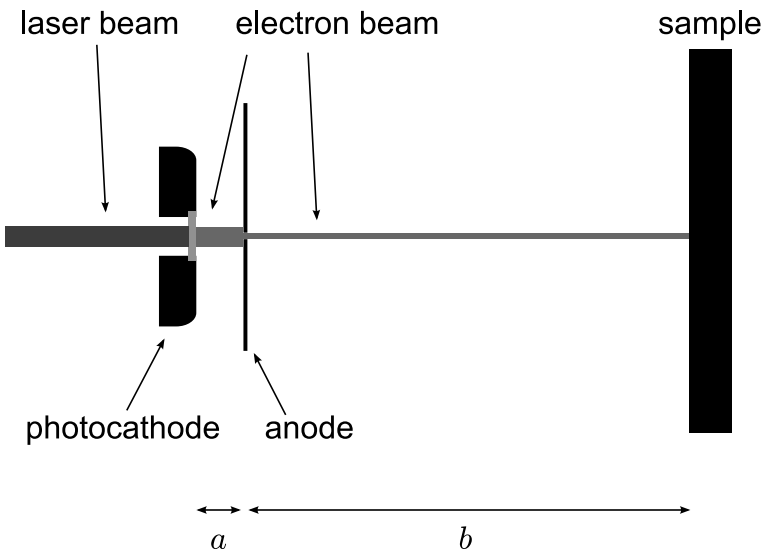

Figure 2.1: A schematic of the electron source. Electrons are extracted from a photocathode by a UV laser beam. They are then accelerated in the electric field between the electrodes and sent to the sample. The electron pulse broadening can be divided into two regions: *(a)* acceleration region; *(b)* drift region.

2.1 Acceleration region

Once an UV laser pulse hits the photocathode, photoelectrons are extracted with an initial kinetic energy distribution that depends on the laser pulse wavelength and the photocathode material properties. The energy of the photoelectrons at the full width at half maximum (FWHM) of the kinetic energy distribution will be:

$$E_0 - \frac{\Delta E}{2} = \frac{1}{2}m(v_0 - \frac{\Delta v}{2})^2 \tag{2.1a}$$

$$E_0 + \frac{\Delta E}{2} = \frac{1}{2}m(v_0 + \frac{\Delta v}{2})^2 \tag{2.1b}$$

Here E_0 is the average kinetic energy of the photoelectrons, ΔE is the FWHM of the initial kinetic energy distribution, v_0 is the average velocity of the photoelectrons, Δv is the velocity spread of the the photoelectrons and e and m_e are the charge and the mass of the electron, respectively.

The velocity spread of the photoelectrons can be calculated from Eq 2.1 as:

$$\Delta v = \sqrt{\frac{2}{m_e}}\left(\sqrt{E_0 + \frac{\Delta E}{2}} - \sqrt{E_0 - \frac{\Delta E}{2}}\right) \tag{2.2}$$

Once extracted, the photoelectrons are accelerated in the a high extraction field (10 kV/mm) (see Fig. 2.1). Since the final electron energy is much bigger then the initial energy, the equation for the pulse broadening time becomes

[Ref. 32]:

$$\Delta t = \frac{\sqrt{2m_e}}{e}\frac{1}{E_{acc}}\left(\sqrt{E_0 + \frac{\Delta E}{2}} - \sqrt{E_0 - \frac{\Delta E}{2}}\right) \tag{2.3}$$

where E_{acc} is the accelerating electric field. If an assumption is made that $E_0 = \Delta E/2$, the Eq. (2.3) becomes [Ref. 33, 34]:

$$\Delta t \approx \frac{\sqrt{2m_e \Delta E}}{e}\frac{1}{E_{acc}} \tag{2.4}$$

This equations gives an estimation for the electron pulse duration after acceleration.

It is important to notice that in this region the temporal broadening of the electron pulses is not a direct function of the acceleration voltage, but of the acceleration field, so it is of great importance to keep the distance between the electrodes as small as possible (see Fig. 2.1). Also, by choosing a photocathode material and a UV laser beam frequency in such a way that the initial kinetic energy distribution of the photoelectrons is as small as possible, the temporal broadening of the electron pulses can be minimized.

In the case of the electron source used in experiments, the photoelectron source was a thin silver film (40nm) and the acceleration field was 10kV/mm, so the estimated pulse duration after acceleration was 300fs.

Electrons spend very little time in the acceleration region (less then 100 ps for 30 kV voltage at 3 mm distance), while in the drift region they spend up to a 1ns (10 cm $\sim$ 1 ns). As a result, the space-charge effect will be taken into account for temporal pulse broadening only in the drift region.

2.2 Drift region

Since electrons enter this region already accelerated to a high velocity, the initial energy distribution does not play a significant role here. The space-charge effect is the main reason for the pulse broadening in this region. The mean field model [Ref. 8] was used to calculate the pulse broadening due to the space-charge effect. This method has already been proven [Ref. 8, 35–37] to give results which are in good agreement with experiments.

2.2.1 Mean field model

The basic concept of this model is to substitute the sum of all Coulomb forces from electron-electron interaction with an effective electric field. To do so, the geometrical properties of a pulse must be determined first. If the electron pulse has a duration of 300 fs after the acceleration and the electrons have an energy of 30 keV, then the length of the pulse will be $\sim$30 μm. The electron beam has a diameter of $\sim$200-300 μm, depending on the diameter of the pinhole and the divergence of the electron beam, allowing each pulse to be represented as a charged disk. The potential on a symmetry-axis (z-axis) for a charged disc is [Ref. 38]:

$$V = \frac{Ne}{2\varepsilon_0 \pi r^2} \left(\sqrt{z^2 + r^2} - z \right) \tag{2.5}$$

Here N is the number of electrons, ε_0 is the vacuum permittivity, r is the pulse radius and z is the distance from the center of the disc.

The force acting on the electron at the beginning of the electron pulse, calculated

from 2.5, is:

$$m\frac{dv_z}{dt}\bigg|_{z=l/2} = \frac{Ne^2}{2\varepsilon_0\pi r^2}\left(1 - \frac{l}{\sqrt{l^2+4r^2}}\right) \tag{2.6}$$

where l is the total length of the pulse in the z direction.

Since the electron pulse has mirror symmetry with respect to the plane normal to the propagation direction and going through the center of the pulse, the electron at the end of the pulse will experience a force of the same amplitude, but with opposite sign. The geometrical length of the electron pulse then changes with time as:

$$\frac{dl}{dt} = 2v_z \tag{2.7}$$

By combining Eq. (2.6) with Eq. (2.7), we have:

$$\frac{d^2l}{dt^2} = \frac{Ne^2}{m_e\varepsilon_0\pi r^2}\left(1 - \frac{l}{\sqrt{l^2+4r^2}}\right) \tag{2.8}$$

This equation was integrated using the leapfrog method (see Appendix A). A result of the calculation is presented in the Figure 2.2.

In the experimental setup the sample is positioned at a distance of 75 mm from the electron source. Fig. 2.3 shows the electron pulse duration at the sample as a function of the number of electrons.

The data can be fitted with a linear function, and this fit can be used for an estimation of the electron pulse duration for the given number of the electrons. The linear fit gives:

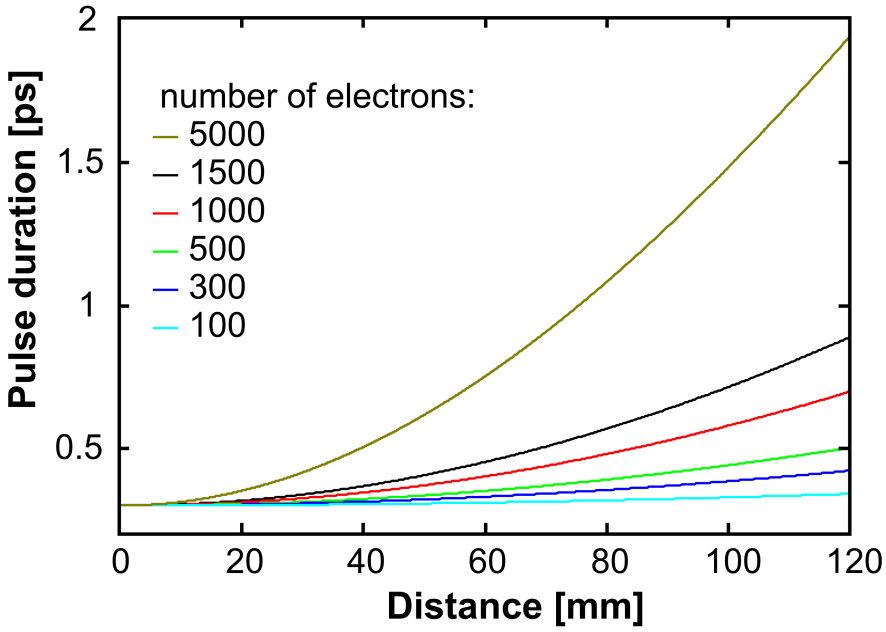

Figure 2.2: The effect of the space-charge on the electron pulse duration as determined by the number of electrons.

$$\tau_{el}[ps] = 0.3 + 1.4 \cdot 10^{-4} \cdot N_{el} \tag{2.9}$$

Here τ_{el} is the duration of the electron pulse in picoseconds and N_{el} is the number of electrons.

The discussion of the electron pulses dynamics showed that, in order to minimize the temporal broadening due to the effect of the initial energy distribution, electrons should be accelerated to high energies in the first few hundred micrometers of their path, thus causing the relative energy difference to become very small. To minimize the influence of the space-charge effects, pulses should contain a low number of electrons (up to a few thousand) and the sample should be placed as close to the electron source as possible.

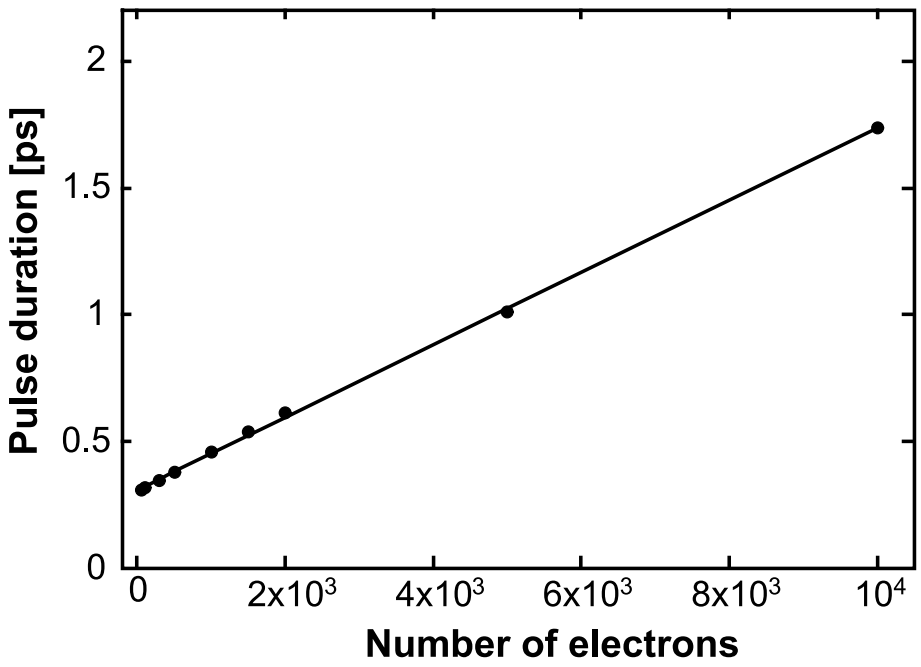

Figure 2.3: Dependence of the electron pulse duration at the sample as a function of the number of the electrons.

As it has been shown here, it is possible to achieve sub-ps electron pulse duration with a few thousand electrons per pulse. The duration depends on both the number of electrons and the drift length. Therefore it is of great importance to keep both of them as small as possible. The sample used for the experiments described in this thesis was at a distance of 7.5 cm from the anode and the experiments were performed with $\sim$2500 e/pulse. Under these conditions pulses had sub-picosecond duration at the sample.

2.3 Divergence of electron pulses

As shown in Figure 2.1, the electrons traveled through the pinhole in the anode. This pinhole induced a change in the electrostatic field between the electrodes so that the equipotential lines in front of the pinhole were no longer parallel to the anode. Due to this effect, the pinhole behaved as a concave lens [Ref. 39, 40]. The pinhole effect was simulated in Simion™, and the result can be seen in Figure 2.4. The pinhole diameter was 100 μm, the distance between the electrodes was 3 mm and the voltage between the electrodes was 30 kV.

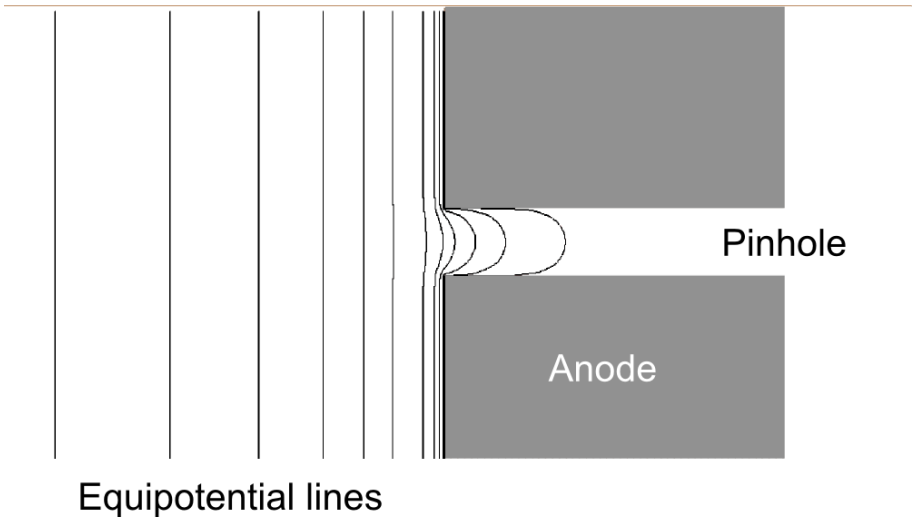

Figure 2.4: The pinhole effect on the electric field near the anode. The equipotential lines in front of the pinhole become non-parallel to the anode, and caused the electrons to diverge.

In Figure 2.5 the defocusing effects of the pinhole are shown, as simulated in Simion™. Electrons were accelerated in the 30 kV/mm electric field for 3 mm, and then passed through the 100 μ pinhole. After passing the pinhole, the beam had a half-angle of divergence of 0.22°. The estimated beam diameter at the 20 cm distance from the pinhole, which was the distance of the MCP detector

screen from the electron source in the experiments, was 4mm.

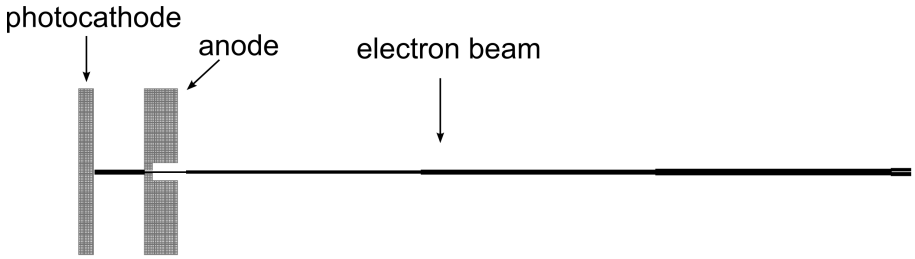

Figure 2.5: The divergence of the electron beam due to the pinhole effect simulated in Simion™ . The half-angle of divergence of them beam after passing through the pinhole is 0.22°.

The defocusing effect of the pinhole can generally depend on several parameters [Ref. 39]:

- electric field strength
- distance between the electrodes
- diameter of the pinhole

Simion™ was used to characterize the influence of these factors on the electron divergence. In simulations, bunches of electrons without any kintic energy were placed in front of a cathode, accelerated towards an anode, passed through a pinhole in the anode and then travelled with constant energy. The dependence of the half-angle of divergence of the electron beam on an accelerating voltage and pinhole diameter was calculated.

For the given distance between electrodes (3mm) and the pinhole diameter (100 μm), the half-angle of divergence of the electrons does not change much with acceleration voltage, only 10% for the voltages from 0.1 to 100 kV, as shown in Figure 2.6. Here, the broadening of the pulse due to the space-charge

effect in the direction normal to the propagation of the pulses was not taken into account.

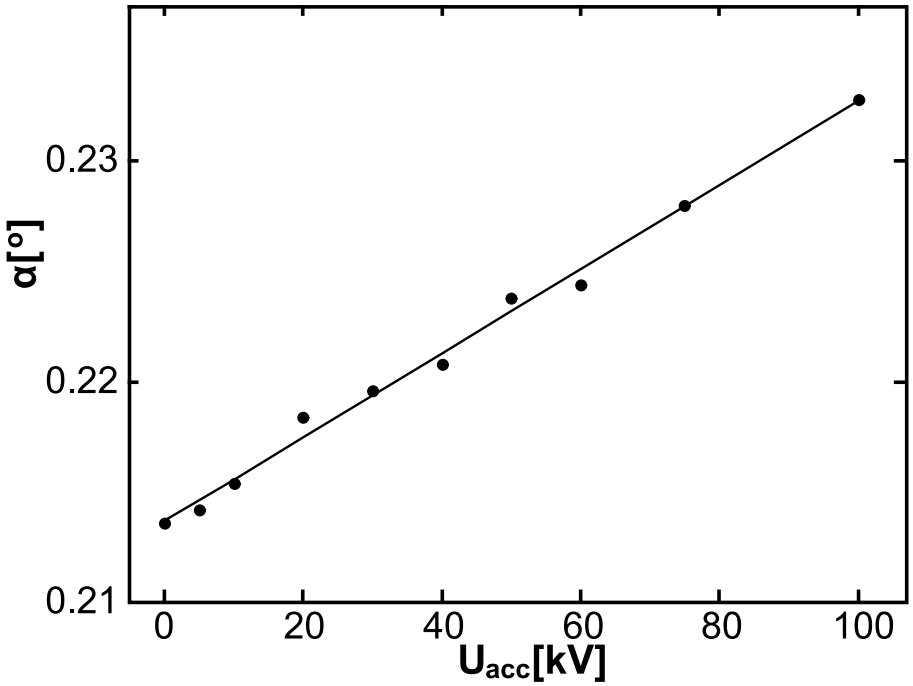

Figure 2.6: The calculated dependence of half-angle of divergence (α) on the acceleration voltage (U_{acc}).

The pinhole diameter has a much larger effect. As shown in Figure 2.7, the half-angle of divergence changes from 0.22° to 2.5° when the pinhole diameter changes from 100 μm to 1 mm.

2.4 Focusing of electron pulses

The pinhole in the anode was changing the geometry of the electric field in such a way that it behaved as a defocusing lens for the electrons. When performing diffraction experiments, it is very important to use a parallel beam, otherwise the Bragg condition for diffraction might not be fulfilled for the non-parallel parts

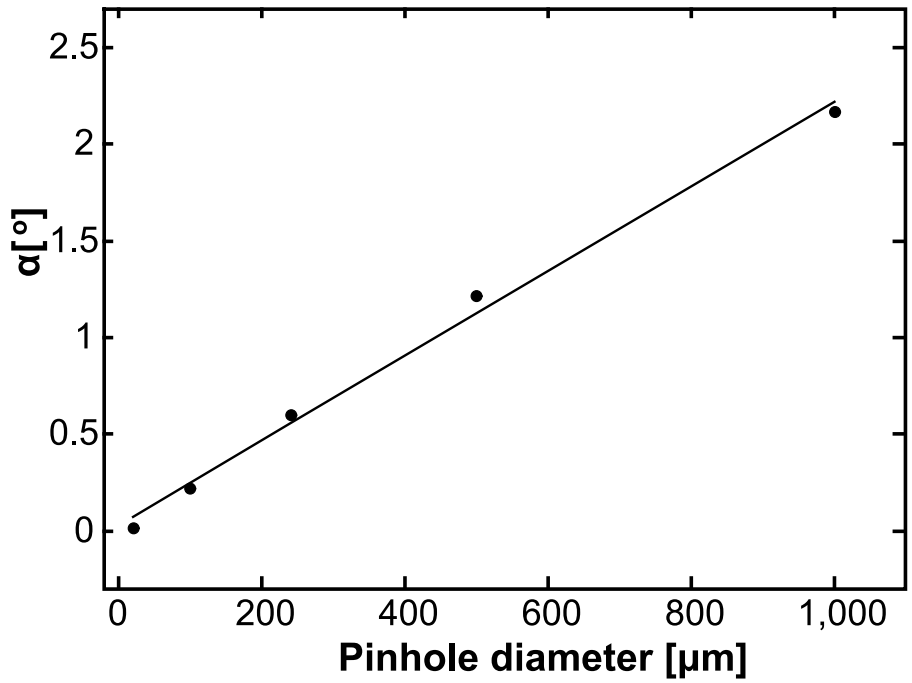

Figure 2.7: The calculated dependence of the half-angle of divergence (α) on the pinhole diameter. The half-angle of divergence changed form 0.22° for a 100 μm pinhole to 2.5° for a 1 mm pinhole.

of the beam. This way, the diffracted intensity will be lower than that in the case of the parallel beam. Also, in order to get sharp diffraction patterns on the detector, the electron beam has to be focused. This can be achieved by using an electrostatic or magnetic lens.

2.4.1 Electrostatic lens

Here a special sort of electrostatic lenses will be discussed, namely an einzel lens (see Fig. 2.8). The einzel lens consists of two outer electrodes connected to the voltage V_1 and an inner electrode connected to the voltage V_2. Insulating spacers between the electrodes prevent electric current and sparking.

In the specific case of the einzel lens built for this experimental setup, the

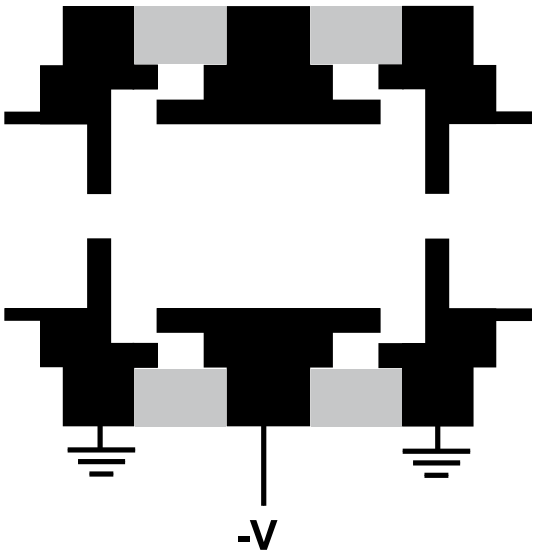

Figure 2.8: Electrostatic lens - einzel lens. The ground electrodes are on the outside and the negative electrode is in the middle. Two insulation spacers are positioned between them.

outer electrodes were grounded, while the inner electrode was connected to an adjustable negative voltage.

Since the lens has the same potential on both sides, electrons will have the same energy at the exit of the lens as they had at the entrance, but theirs trajectories will be changed in such way that they converge on to the axis [Ref. 39]. However, due to the uneven deceleration and acceleration of the electrons inside the lens and the different path lengths, the electrons will not spend the same amount of time inside the lens, causing the electron pulse to be longer after passing through the lens. The focusing properties of the lens depend on the electron energy, negative electrode voltage and lens geometry. The results of the einzel lens simulation will be presented in Chapter 3.

The electrostatic lens that was first used in this setup had a radius of 1 cm and

a length of 2.5 cm, and could sustain a voltage of up to -12 kV to the negative electrode without sparking. Sparks appeared at higher voltages. After initial tests, the electrostatic lens was replaced by a magnetic lens.

The advantages of a magnetic lens in comparison with a electrostatic lens when used for ultrafast electron diffraction are:
- a magnetic lens does not require a high voltage for operation;
- since a magnetic field does not change the energy of the electrons but just their trajectories, there is no additional temporal broadening of the electron pulses inside the magnetic lens.

2.4.2 Magnetic lens

Figure 2.9 shows a schematic of a magnetic lens A magnetic lens consists of a coil of insulated wires inside a hollow cylinder with a hole along its rotational axis. The cylinder walls are made out of a material with high magnetic permeability, usually iron or steel. Wire is wound around a material with low magnetic permeability, e.g. copper. This way, the magnetic field exists only in the central region of the magnetic lens.

A current through the coils creates a magnetic field in the central part of the magnetic lens. The rotationally symmetric magnetic field is inhomogeneous in such a way that it is weak in the center of the hole and becomes stronger outside the center. Electrons close to the center are less strongly deflected than those passing through the lens far from the axis. The overall effect is that a beam of parallel electrons is focused into a spot (so-called cross-over).

The magnetic field in the center of the magnetic lens can be approximated

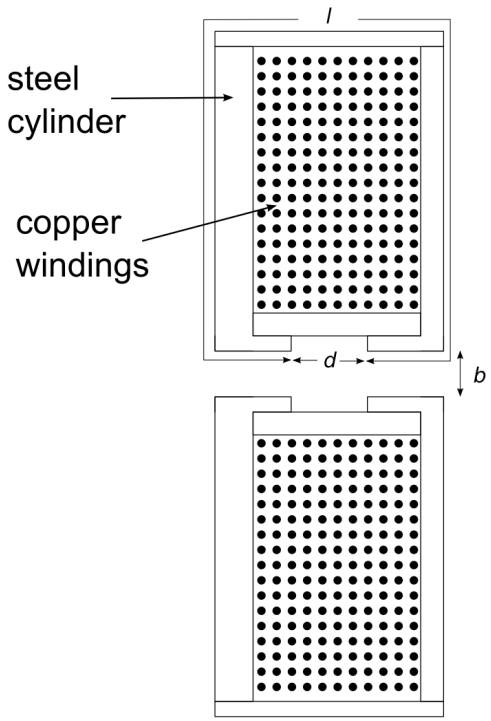

Figure 2.9: Schematic of a magnetic lens. The copper windings are inside the steel cylinder. The inner diameter of the lens is b, and the gap in the cylinder is d. l is the perimeter of the one side of the cylinder without the length of the gap d.

by [Ref. 40]:

$$B = \frac{\mu_0 I N}{d + \frac{l}{\mu}} \tag{2.10}$$

where μ_0 is the vacuum permeability, I is the current through the coil, N is the number of windings, d is the length of the gap in the cylinder hole, l is the perimeter of the one side of the cylinder without the gap d (see fig 2.9) and μ is the relative permeability of the pole (see figure 2.9). Equation 2.10 is valid for $b \leqslant d$ (b is the diameter of the hole in the cylinder.)

The relative permeability of the steel is in the range of 600 to 1000, so the $\frac{l}{\mu}$ term can be neglected from the equation (2.10), which gives:

$$B = \frac{\mu_0 IN}{d} \tag{2.11}$$

When electrons travel through the magnetic lens, they are affected by the Lorentz force:

$$\overrightarrow{F} = -ev \times \overrightarrow{B} \tag{2.12}$$

Thus, the electrons whose trajectories are going through the center of the lens and are parallel with the magnetic field will not be affected by the magnetic lens. For all other electrons, the Lorentz force will change their velocities in such a way that they will start converging towards the central axis of the magnetic lens (see Fig. 2.10).

The focal length of the magnetic lens is [Ref. 40]:

$$f_0 = \frac{4m_e^2 v_0^2}{e^2 \int_{-\infty}^{\infty} B_z^2 dz} \tag{2.13}$$

where m_e is the mass of the electron, v_0 is the electron velocity, e is the electron charge and B_z is the magnetic field in the z direction (the direction of the electron propagation).

By substituting the value for B from Eq. (2.11) into Eq. (2.13) and using the approximation that the magnetic field is constant in front of the gap in the cylinder and equal to zero everywhere else, the integral of the magnetic field will

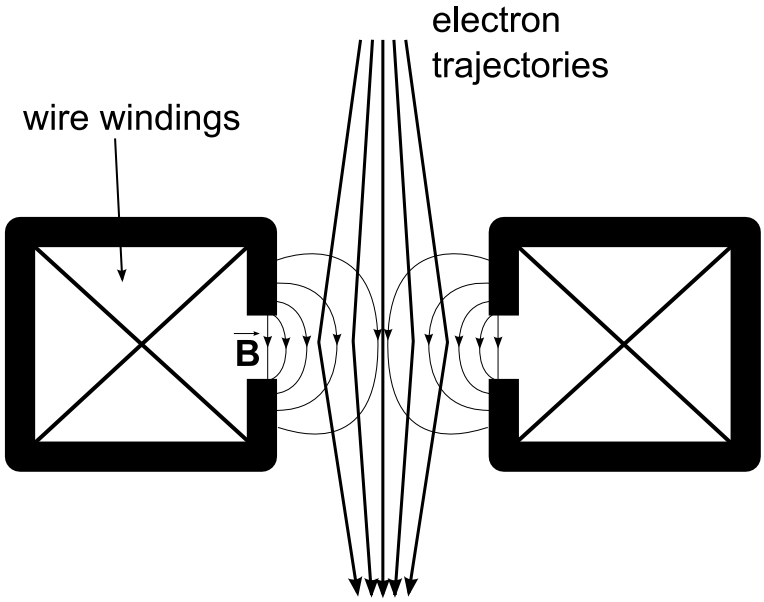

Figure 2.10: Focusing of electrons with a magnetic lens. Electrons traveling on the axis of the magnetic lens remain on their trajectory. Electrons traveling off-axis are focused by the Lorentz force.

be:

$$\int_{-\infty}^{\infty} B_z^2 dz = B_z^2 d \tag{2.14}$$

and finally the focal length will be:

$$f_0 = \frac{4dm_e^2 v_0^2}{e^2 \mu_0^2 I^2 N^2} \tag{2.15}$$

If the equation is rewritten so that IN is on the left side, it will give:

$$IN = \sqrt{\frac{4dm_e^2 v_0^2}{e^2 \mu_0^2 f_0}} \tag{2.16}$$

This equation shows the relation for electrical current and number of windings needed to focus the electrons.

Based on this equation and on the parameters of the experimental setup, a magnetic lens was built. It had a radius of 4.5 cm, it was 3 cm long and had 800 wire windings. The wire used for this purpose was an insulated copper wire, 1 mm in diameter.

Although the magnetic lens does not induce temporal broadening of the electron pulses by changing the energy of the electrons traveling through it, like an electrostatic lens does, the electron pulses can still temporally broaden due to the different paths they travel. For the small angles of divergence of the beam, this broadening is in the range of 10 fs and can be neglected in respect to the space-charge effect.

Chapter 3

Characterization of the electron source

In this chapter, the characterization of the electron pulses will be discussed. As previously stated in Chapter 2, electron bunches are produced at the photocathode, accelerated in the high electric field between the electrodes and then focused with an electrostatic or a magnetic lens. Since a low number of electrons per pulse is important for achieving high temporal resolution (as shown in 2.2.1), the experimental determination of the numbers of electrons in an individual pulse is necessary.

First, the experimental setup will be described. Then, the method for determining the number of electrons per pulse will be presented. Following this, the divergence of the electron beam due to the lens effect of the pinhole will be discussed, as well as the focusing properties of both the electric and magnetic lens.

3.1 Experimental Setup

3.1.1 Electron source

The electron source consists of a photocathode, an anode with a pinhole and a lens for the collimation of electrons. The photocathode is illuminated from the back with a laser pulse to produce photoelectrons. These electrons are then accelerated by the electric field between the electrodes. When accelerated, their initial kinetic energy can be neglected compared to the final energy ($\sim$1 eV to 30 keV), so the electron velocity component transversal to the accelerating field can also be neglected. Thus the electron beam can be regarded as parallel. After passing through the pinhole, the electron beam becomes divergent. The collimating lens is placed after the anode in order to collimate electrons.

The sample is mounted on a sample manipulating system which has 3 degrees of freedom: translation in the plane normal to the electrons propagation direction and rotation around the vertical axis.

Once electrons are diffracted, they arrive at the multichannel plate (MCP) detector, which is at a distance of 19.2 cm from the sample. The MCP detector is in the Chevron configuration and has a phosphor screen with P20 phosphor which emits a green light signal with a peak at 530 nm. Diffraction patterns are then recorded with a 12-bit CCD camera, which has 70% quantum efficiency for wavelengths between 450 and 550 nm.

Figure 3.1 shows a schematic of the model of the electron source, while in Figure 3.2 a photo of the electron source can be seen.

A Macor holder is mounted onto a metal construction. A Rogowski profile

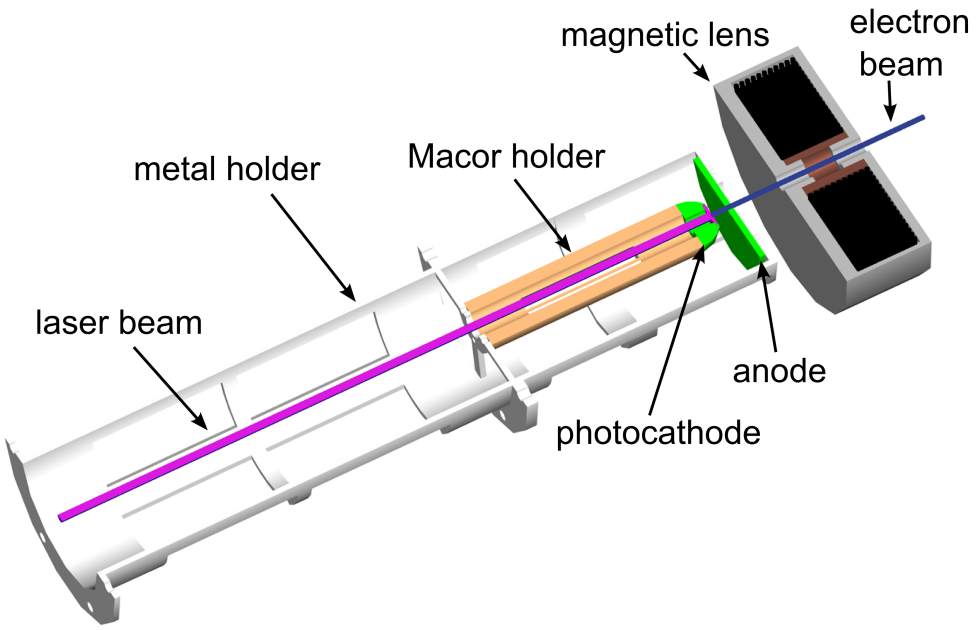

Figure 3.1: Schematic of the electron source. The Macor holder with the photocathode on its top is mounted on the cylindrical metal holder. The anode with a pinhole is connected to the top of the metal holder. The magnetic lens is placed after the anode. A laser beam for producing photoelectrons is also shown.

cathode is positioned on top of the Macor holder and holds the photocathode. The anode with the pinhole is not shown in this photo.

Photocathode

For the acceleration of the electrons between the electrodes, a uniform electric field is desirable. The ideal way of achieving this would be with two flat plates of sufficiently large extension. Finite sized plates can create a uniform field at the middle of the plate, but the outer region of the plates tends to generate a higher field which can create a problem, therefore limiting the highest achievable

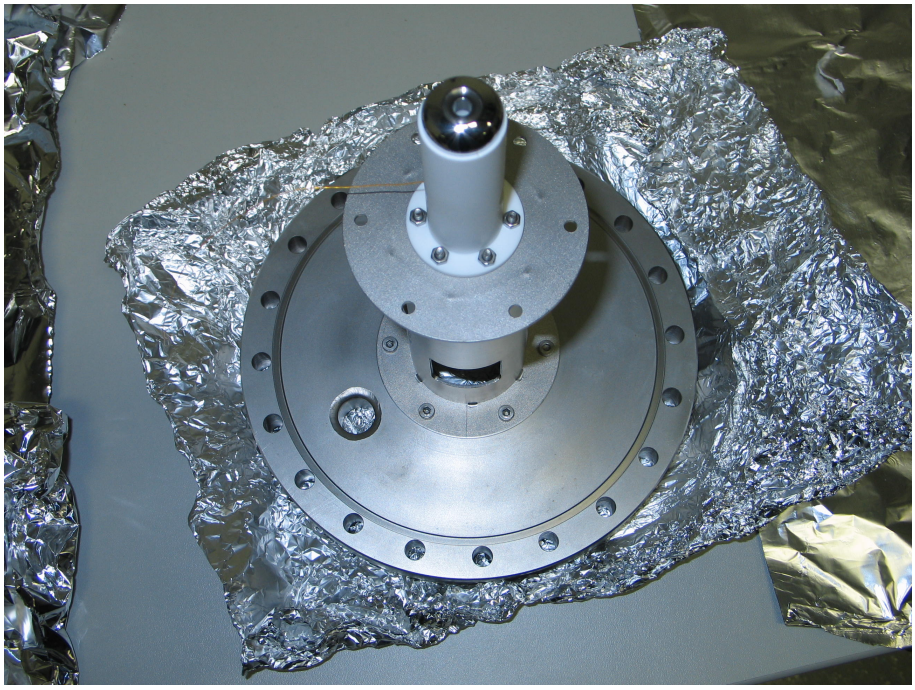

Figure 3.2: Photo of the electron source. Second part of the metal holder with the anode is not connected.

voltage in the central region. The solution to this problem would be to have an electrode with a flat central area which provides a uniform field, and a curved edge surface shaped in such a way that the electric field is lower than that in the central region. As calculated [Ref. 41–43], one of the best ways to construct the curved edge with this characteristic is to use the Rogowski profile.

The negative electrode that was used for this electron source had a flat central part and a well-polished Rogowski profile at the edge. The distance between the photocathode and the anode was 3 mm, and a voltage of 30 kV could be applied without breakdown. Thus, the acceleration field was 10 kV/mm.

The photocathode was prepared by evaporating a thin silver film (40 nm) on top of the sapphire substrate and a tungsten film ($\sim$200 nm) on the back (see Fig.

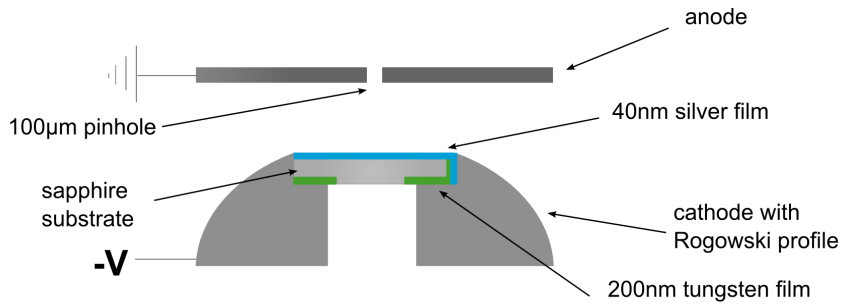

Figure 3.3: The photocathode and the anode with a pinhole. The distance between them is 3 mm. There is a 40 nm silver film on the top and on the right side of the sapphire, and a ∼200 nm tungsten film on the right side and on the bottom of the sapphire.

3.3). These two films were overlapping on the side, thus providing the electric contact of the silver film with the back side of the sapphire. When depositing the tungsten, a mask was placed over the center of the substrate so that UV laser pulses for the production of photoelectrons would not be blocked by the tungsten. The photocathode was then inserted into a corresponding opening in the body of the cathode. Liquid silver was used to connect these two parts and also to provide electric contact between the electrode and photocathode.

In order to generate photoelectrons from the silver film, the laser pulse with energy higher than the work function of the thin silver film (3.7 eV) [Ref. 44] was needed. The third harmonic pulses of a Ti:Sapphire laser pulses (267 nm, 4.65 eV) were used for the generation of photoelectrons.

3.1.2 Laser system

The ultrafast laser system used was a Ti:Sapphire amplifier system based on the Chirped-pulse amplification (CPA) [Ref. 1, 2, 45, 46] technique. In order to pre-

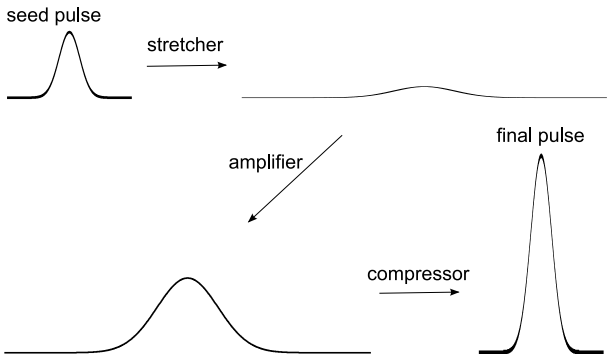

Figure 3.4: The temporal pulse shape in different parts of the chirped-pulse amplifier. The final pulse intensity is few orders of the magnitude larger than the seed pulse intensity.

vent the nonlinear effects that could induce pulse distortion or damage to the gain medium, the pulses are temporally stretched in a device called a stretcher before passing through the amplifier medium. The stretcher is a dispersive element and has a positive group velocity dispersion (GVD). After amplification, a compressor with an negative GVD is used to remove the chirp and temporally compress the pulses to a duration similar to the input pulse duration. The temporal pulse shape in different stages of the chirped-pulse amplification is shown in Fig. 3.4.

The Ti:Sapphire laser system consists of the following parts (see Fig. 3.5):

- femtosecond oscillator
- stretcher
- three amplification stages
- compressor.

A CW Nd:VO_3 laser with 3.6 W average power at 532 nm was used for

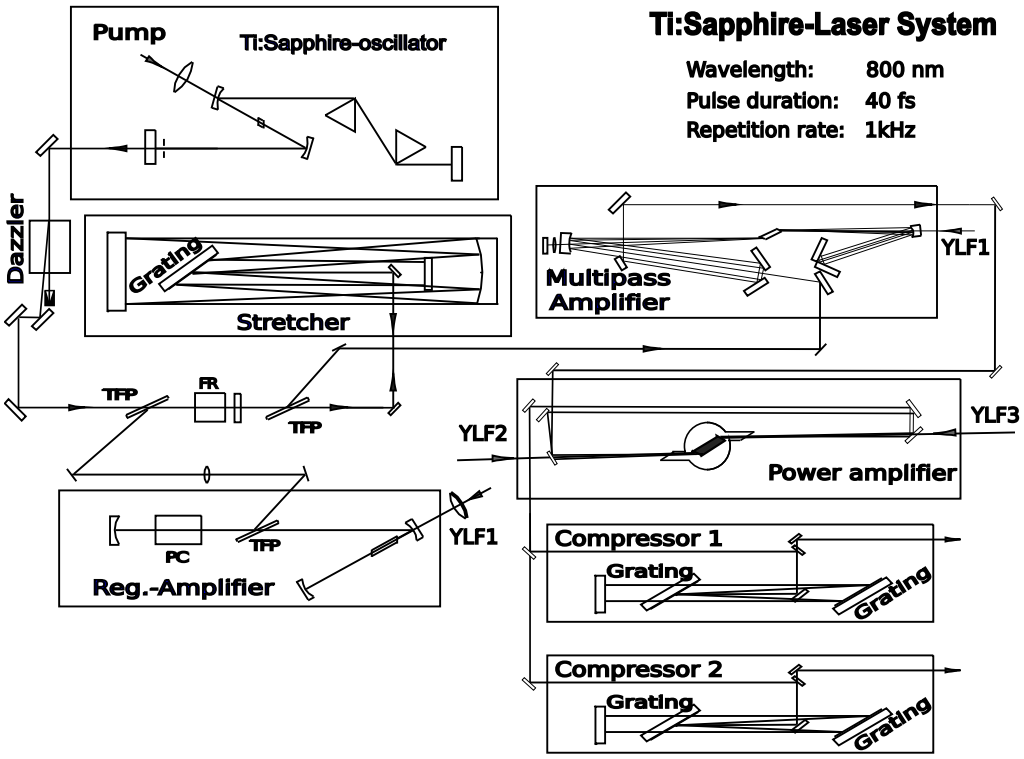

Figure 3.5: Schematic of the laser system.

pumping the mode-locked Ti:Sapphire laser oscillator. The oscillator delivered 20 fs pulses with an average power of 100 mW at a 82 MHz repetition rate.

In the laser system presented in Fig. 3.5, a grating and a mirror were used as a stretcher. A temporal pulse broadening of 4 orders of magnitude was induced, from 20 fs to 170 ps. At the same time, the peak pulse power was lowered by the same factor.

For amplification, three amplification stages were used, pumped with three Nd:YLF lasers.

The first amplification stage was the regenerative amplifier, where each pulse made 20 round trips and was amplified to 600μJ pulse energy. From the re-

generative amplifier, the pulses went to the first multi-pass amplifier. There the pulses were amplified to 2.2 mJ by passing 4 times through the Ti:Sapphire crystal. The final amplification stage was the second multi-pass amplifier, where pulses passed twice through the Ti:Sapphire crystal. Finally, the pulses were compressed in the compressor.

After compression, the pulses had a maximal energy of 5 mJ power and a 40 fs duration. The repetition rate of the laser system was 1 kHz.

3.2 Experimental setup

The primary components of the experimental setup were positioned inside a vacuum chamber ($p \approx 10^{-8}$mbar). They consisted of: an electron source, a magnetic lens, a sample positioning system and an MCP detector. A schematic of the setup is presented in Figure 3.6.

The Ti:Sapphire laser pulses are frequency tripled by 2 BBO (β-barium borate, β-BaB_2O_4) crystals. In the first BBO crystal the frequency doubling (or the second harmonic generation, SHG) of the 800 nm beam is performed, and the 400 nm beam is generated. The 800 nm and the generated 400 nm beams then enter the second BBO crystal and, in the process of the sum frequency generation (SFG), generate the 267 nm beam. This beam is guided to the photocathode in order to produce electrons.

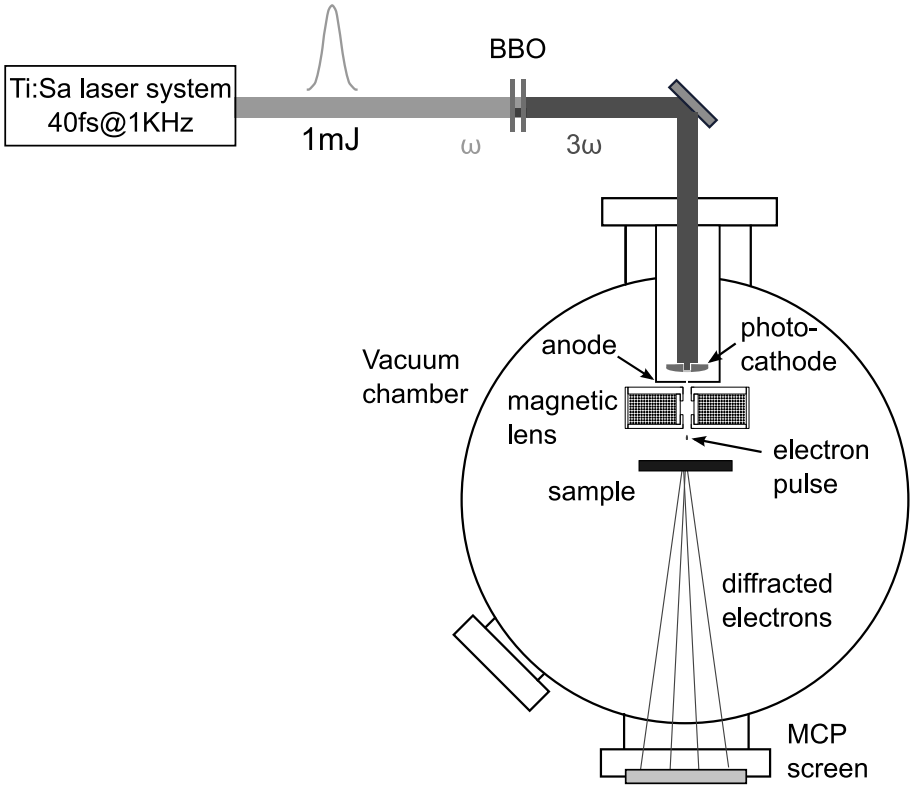

Figure 3.6: Experimental setup. The laser system delivers 40 fs pulses which were frequency tripled by 2 BBO crystals. The third harmonic beam was then sent into the vacuum chamber. The electron source with the magnetic lens was mounted onto the inner side of the CF150 flange. The MCP detector screen was placed at the opposite side of the chamber. The sample was placed in the middle of the chamber.

3.3 Focusing of electron pulses

3.3.1 Focusing with an electrostatic lens

As previously stated in Chapter 3.1, one of the devices used for focusing the electron beam was an electrostatical einzel lens. The equipotential lines within the lens are shown in Figure 3.7.

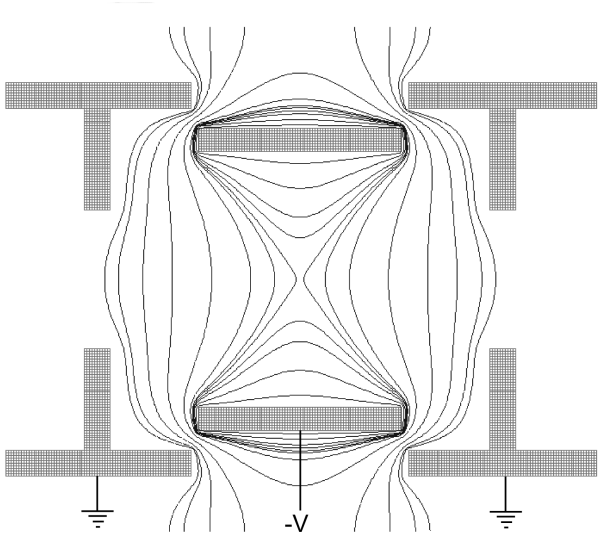

Figure 3.7: The equipotential lines within the electrostatic lens.

For the characterization of the electrostatic lens the dependence of the optimum lens voltage on the electrons energy was determined. The electron pulses were best focused when the voltage on the central electrode had a value of 80% of the electrons' acceleration voltage (see Fig. 3.8).

Without focusing, the electron pulse with E_{kin}=3.7 kV had a FWHM of 4 mm at the MCP detector. This value is in the good agreement with the Simion™ simulation. With the electrostatic focusing the FWHM diameter could be reduced to 0.7 mm (Fig 3.9)

From the electric field distribution shown in Fig. 3.7, it is clear that the electrons traveling through the center of the lens will be less decelerated than the electrons traveling off center. Due to this velocity difference inside the lens, the electron pulse will be temporally stretched by the lens. Simulation of the focusing of the electrons with the electrostatic lens showed that this pulse broadening would make the pulses longer than 1 ps. Since the goal of the experiment was to

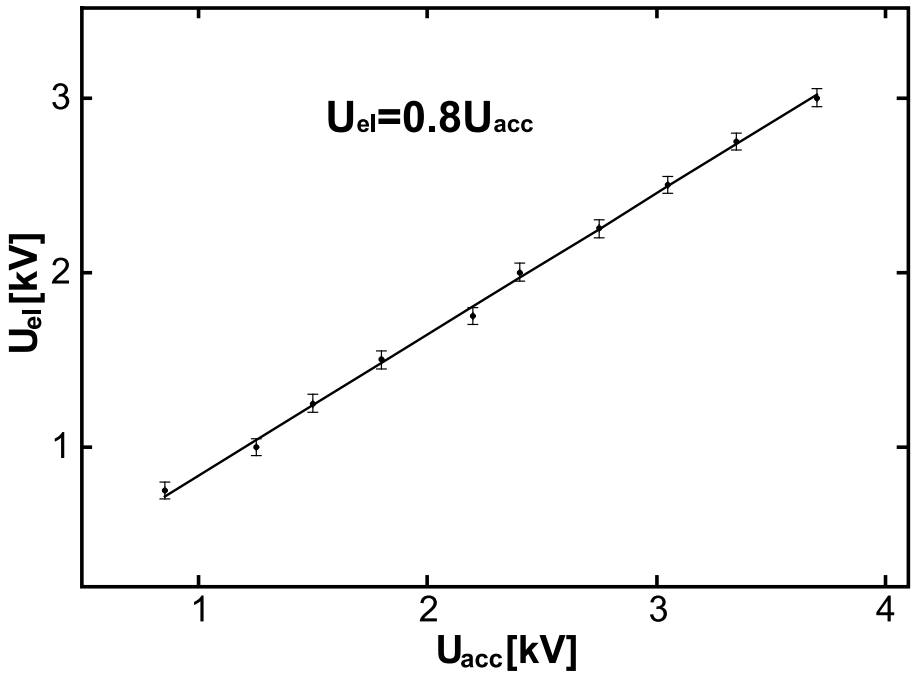

Figure 3.8: Relation between the acceleration voltage (U_{acc}) and the electrostatic lens voltage (U_{el}) needed for the focusing of electron pulses

have sub-ps pulses, electrostatic focusing turned out to be inadequate.

3.3.2 Focusing with a magnetic lens

The magnetic lens was placed directly after the pinhole. The magnetic lens had a 800 rounds of insulated copper wire, it was 3 cm long and had a radius of 4.5 cm. The current needed to focus the electrons was in the range of 1.2-1.4 A, depending on the number of electrons per pulse. For the pulses with a higher number of electrons, a stronger magnetic field was necessary in order to compensate for the larger transversal broadening of the pulse due to the space-charge effect.

When using a magnetic lens in the vacuum chamber, two problems can oc-

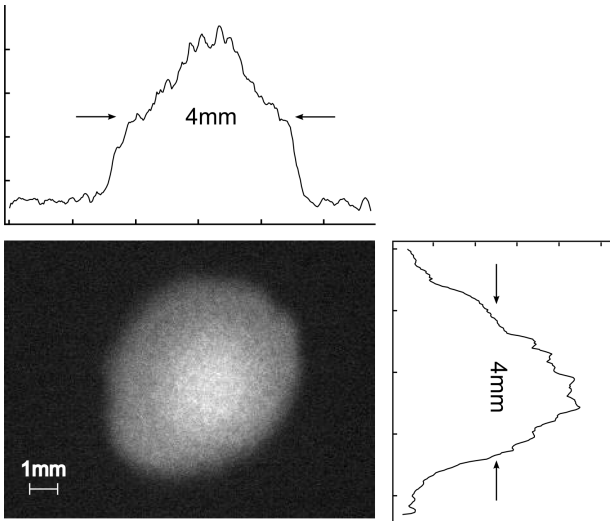

(a) Unfocused electron spot on the MCP

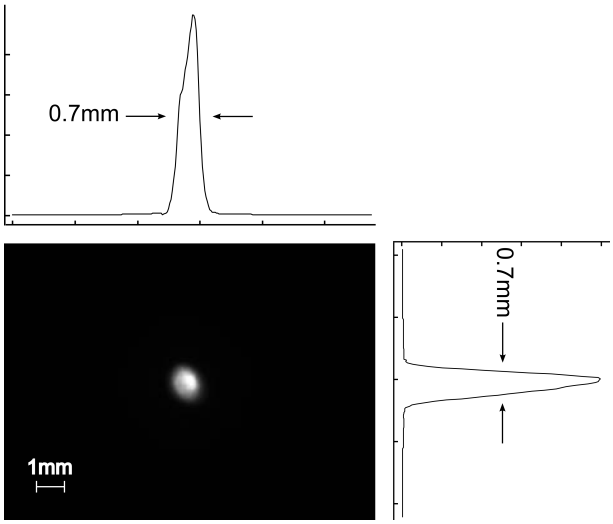

(b) Focused electron spot on the MCP

Figure 3.9: Effect of the electrostatic focusing on the electron spot size on the MCP. The focused spot (b) has a FWHM which is 6 times smaller than the unfocused spot (a).

cur: outgassing and heating.

The wire used for windings was an insulated copper wire and there was some outgassing when the lens was switched on. However, the lens was made with

several holes to increase the pumping cross-section and as a result there were no problems with the vacuum quality due to the outgassing; the pressure in the vacuum chamber was $10^{-7} - 10^{-8}$ mbar.

The magnetic lens has an electric resistance of 2.1 Ω, and for the currents necessary for focusing, the power dissipation was 3-4 W. To ensure that the magnetic lens would not overheat and destroy the copper wire insulation (which melts at $\sim$ 80°C), the thermal contact between the lens and the chamber was made such that the chamber served as a heat sink. A thermocouple sensor was attached to the lens for constant monitoring of the temperature. During the experiments, the temperature increased to a maximum of 37 °C.

Eq. (2.16) can be rewritten as:

$$I = \frac{1}{N}\sqrt{\frac{8dm_e E_{kin}}{e^2\mu_0^2 f_0}} \tag{3.1}$$

According to Eq. 3.1 the current needed to focus the electrons should be proportional to the square root of the electron kinetic energy. Fig. 3.10 shows the measurement of this dependence.

The size of the focus of the electron beam as a function of the lens current and the electron energy was also measured. The data are shown in Fig. 3.11.

It can be noticed in Fig. 3.11 that the electrons with lower energy produced a bigger spot on the MCP. This could be explained by the longer travel time to the MCP. During this time, the space-charge forces influence the electrons not only in the direction of the propagation, but also in the normal direction. The effect in the normal direction was smaller than the one in the propagation direction because the electron pulse had a diameter of 200-500 μm, while the

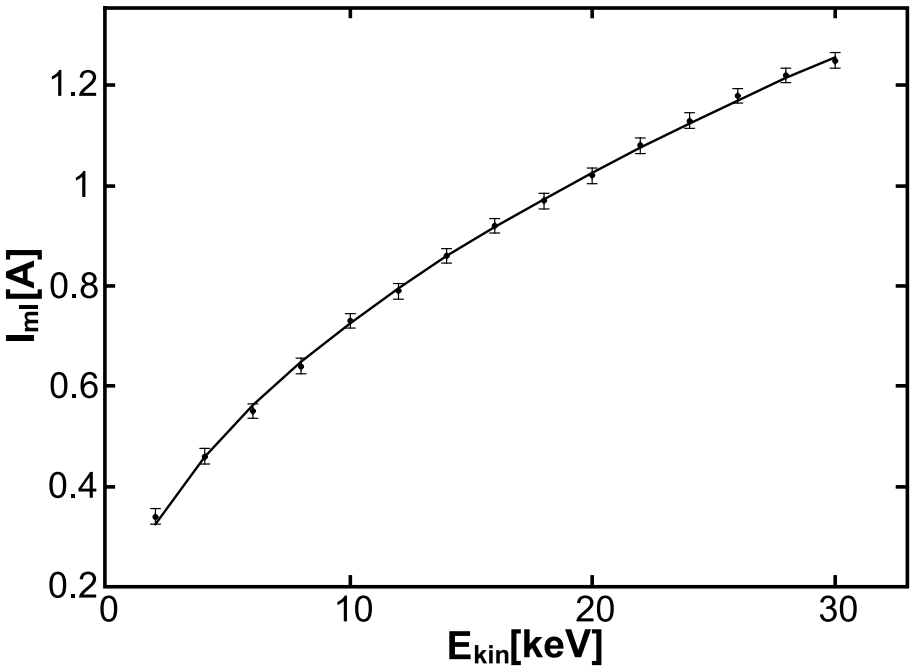

Figure 3.10: Measurement of the magnetic lens current I_{ml} needed for focusing the electrons with the kinetic energy $E_{kin.}$. The points were fitted with the square function, $I_{ml} = a\sqrt{E_{kin.}}$

length of the pulse, for a 500 fs pulse duration, was only 50 μm. Thus, the space-charge effects were much more pronounced in the propagation direction. Since 20 kV and 10 kV electrons spent more time in the drift region than the 30 kV electrons, it is expected that the spots on the MCP would also be bigger for the slower electrons. Also, as presented in Fig. 3.10, the electrons with higher energy required higher magnetic lens currents for focusing, and the electrons with lower energy produced larger focused spots on the MCP. The reason for this behavior is the same as for the spot size without focusing, i.e. slower drift velocity.

The optimally focused 30 keV electron beam with a horizontal and a vertical

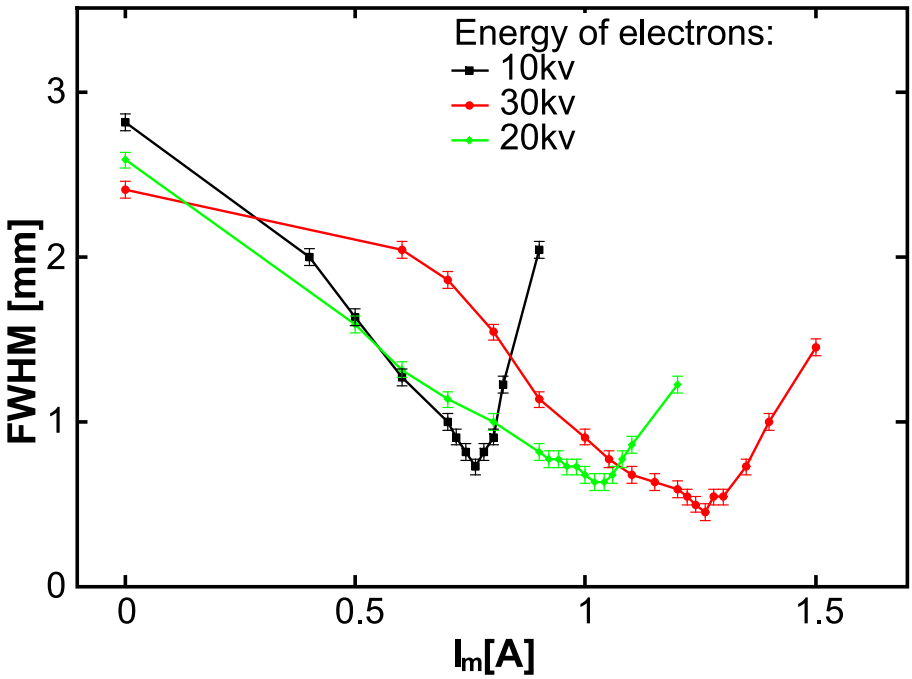

Figure 3.11: The FWHM of the electron spot on the MCP screen as a function of the magnetic lens current.

beam profile is shown in Fig 3.12.

The electron spot on the MCP for different currents of the magnetic lens is presented in Figure 3.13.

The spot became elliptical for smaller currents, but in the focus it had a circular shape. For currents higher than the optimum focusing current, the spots had an irregular shape and were smeared in the vertical direction. In Fig. 3.13(a), on the left side of the electron spot, a smaller spot can be seen. This was part of the 3rd harmonic beam passing through the photocathode and the pinhole.

It can be seen that the focus size remained almost constant for the lens currents of 1.24 to 1.26 A, so the stability of the magnetic lens current of 10 mA would be sufficient for performing experiments. However, the focused electron

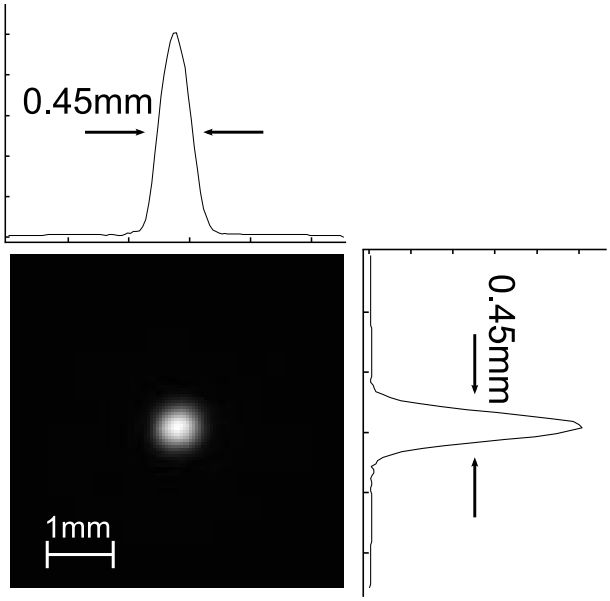

Figure 3.12: The optimally focused 30 keV electron beam. Both vertical and horizontal profiles are shown. FWHM of the beam in both directions is 0.45 mm

spots for 1.24 A and 1.26 A had different positions on the detector screen. The position change of 10 pixels was observed on the CCD camera. In order to stabilize the focused beam position to within better than one pixel, the stability of the lens current should be better than 2 mA.

3.4 Determining the number of electrons per pulse

A technique for determining the number of electrons per pulse was developed, similar to the one presented in [Ref. 47].

As previously discussed in Chapter 3.1, electrons were detected with the MCP detector, and its signal was recorded with the CCD camera. In order to determine the number of electrons per pulse, the contribution of one electron to the detected signal had to be determined. The following is the procedure used to measure the

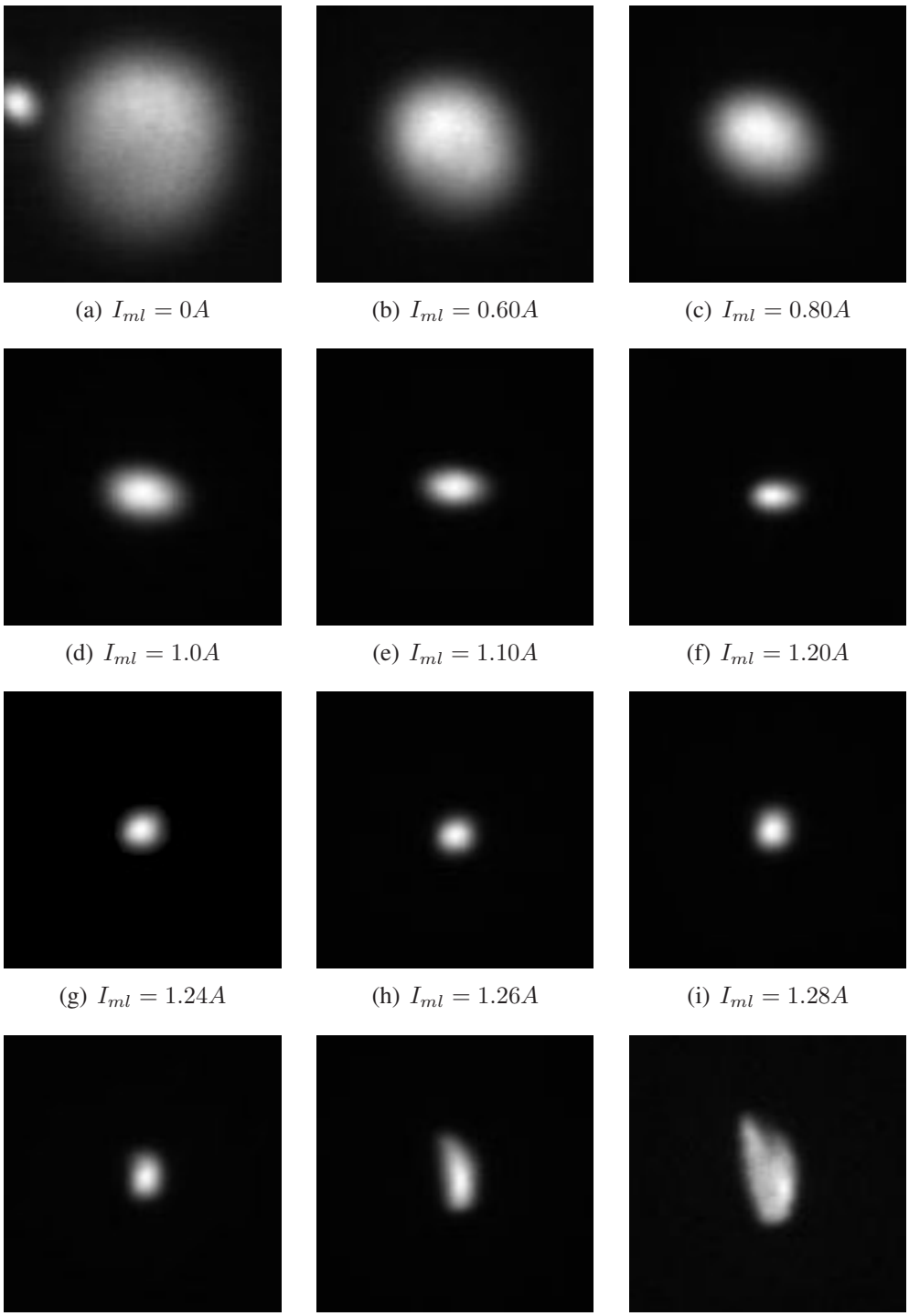

(a) $I_{ml} = 0A$ (b) $I_{ml} = 0.60A$ (c) $I_{ml} = 0.80A$

(d) $I_{ml} = 1.0A$ (e) $I_{ml} = 1.10A$ (f) $I_{ml} = 1.20A$

(g) $I_{ml} = 1.24A$ (h) $I_{ml} = 1.26A$ (i) $I_{ml} = 1.28A$

(j) $I_{ml} = 1.30A$ (k) $I_{ml} = 1.40A$ (l) $I_{ml} = 1.50A$

Figure 3.13: The electron spot on the MCP screen focused by different magnetic lens current. The 3rd harmonic laser beam is visible in the first image.

counts produced by a single electron.

First, the amplification of the MCP was set so that individual electrons could be detected. In this case, a voltage across the MCP plates of 1.5 kV was sufficient for this purpose. Then, the third harmonic intensity was lowered so that each pulse consisted of a low number of electrons (15-25, see Figure 3.14). Due to the shot-to-shot fluctuations of the number of electrons, a series of pictures of individual pulses was taken (CCD camera exposure was set to 0.99ms).

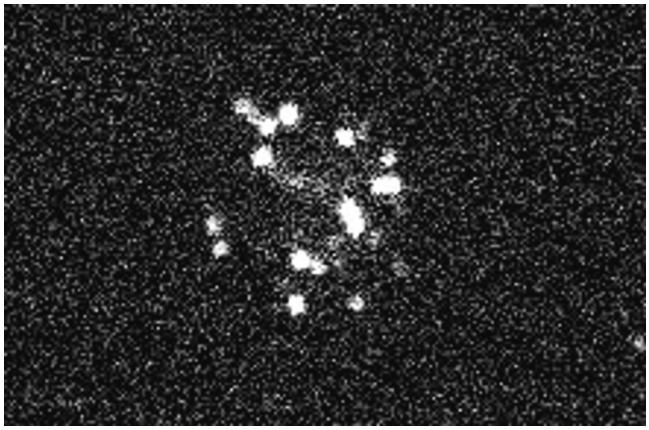

Figure 3.14: Picture of the MCP signal of one electron pulse. The signal from individual electrons can be distinguished.

Each picture was individually treated to determine the signal intensity from individual electrons. The intensity was measured for 250 electrons, and the corresponding histogram is shown in Fig 3.15. The data were fitted with the log-normal distribution [Ref. 48]. The peak value and the mean value of the distribution were 231 and 271 counts, respectively.

By dividing the total intensity of the electron spot by the mean intensity corresponding to one electron, it was possible to determine the mean number of electrons per pulse.

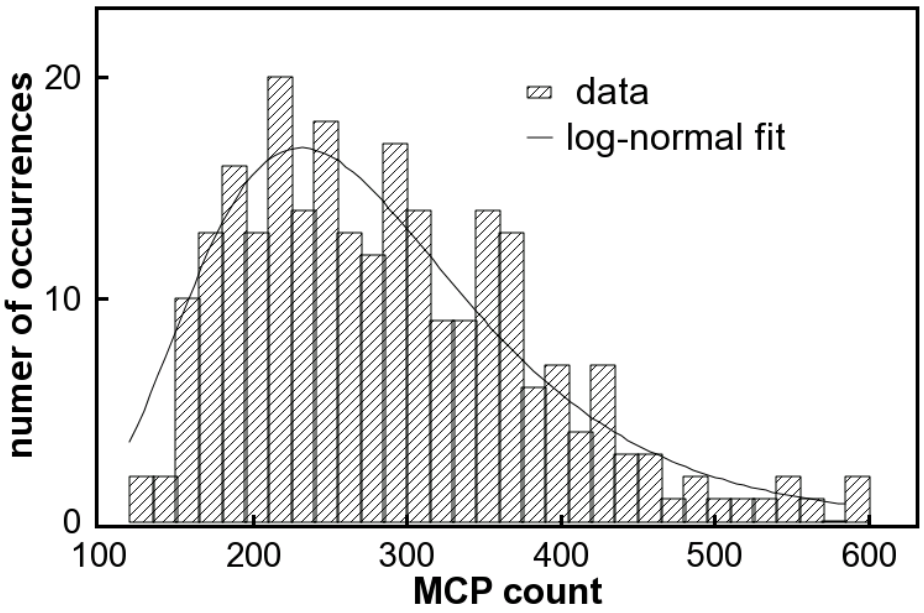

Figure 3.15: Histogram of the MCP counts produced by one electron.

Then, the MCP plate voltage was lowered, first to 1.4 kV and then to 1.3 kV, and the pictures of the electron spot were recorded for both voltages. At these lower voltages, it was no longer possible to see individual electrons, and the exposure of the CCD camera was set to a longer time (10-100ms). During this time, the third harmonic intensity was not changed so there was the same number of electrons per shot as for 1.5 kV MCP plate voltage. By measuring the total intensity of the electrons spot on the picture and using the mean number of electrons per pulse that was already measured, it was possible to determine how many counts are produced by each electron.

The data for counts per electron for different MCP plate voltages are shown in Table 3.1.

Table 3.1: Counts per electron for different voltages of the MCP plate

MCP plate voltage [kV]	counts per electron
1.5	287
1.4	48
1.3	7

Once the number of electrons per shot was determined, the yield of the electron source with respect to the energy of the third harmonic could be measured. This is shown in Figure 3.16.

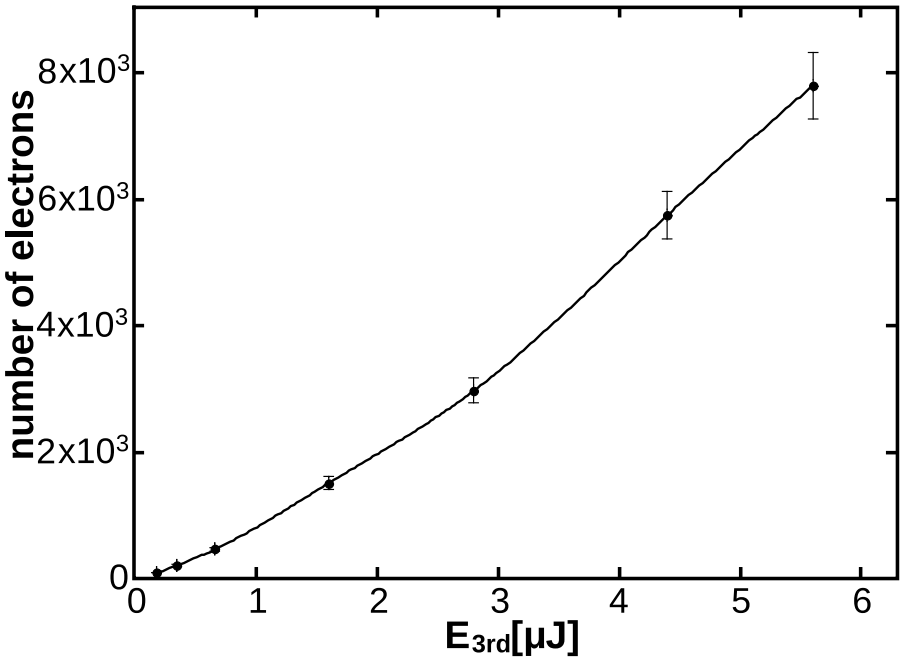

Figure 3.16: Correlation between the number of electrons per pulse and the energy of the third harmonic pulse.

It is important to notice that the data shown in the Table 3.4 correspond to the number of detected electrons. The MCP detector in the Chevron configuration has a nominal detection efficiency of 35% [Ref. 49, 50]. This must be taken into account when determining the total number of electrons per pulse.

Chapter 4

Theoretical introduction to the electron diffraction

This chapter will address the basics of the diffraction theory [Ref. 51–53]. First, the conditions for forming diffraction patterns will be explained and then the effect of the sample thickness on the diffraction conditions will be considered. Finally, the dependence of the diffracted intensity on the sample temperature will be discussed.

4.1 Bragg's law

When X-rays are reflected from lattice planes (see Fig 4.1), they can produce either constructive or destructive interference.

The interference will be constructive only if the path difference between two waves is equal to the multiple of their wavelength. If the distance between two planes is d, and the incident waves are coming with the angle θ, then the condi-

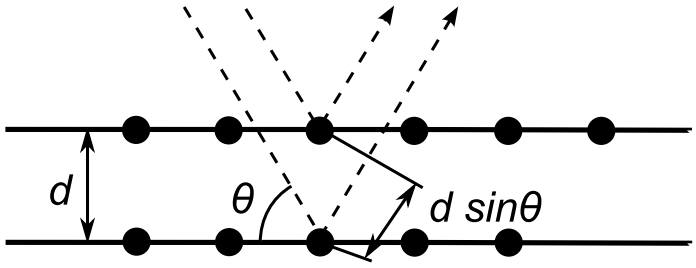

Figure 4.1: Waves reflecting from parallel lattice planes.

tion for the constructive interference is:

$$n\lambda = 2d \cdot sin\theta \tag{4.1}$$

This equation [4.1] is known as the Bragg's law [Ref. 54]. It was first used to explain the interference pattern of X-rays scattered by crystals, but it can be used for describing the diffraction of any beam (ions, electrons, neutrons, and protons) with samples in all states of matter. The only important point is that the beam should have a wavelength comparable to the distance between the atomic or molecular structures of interest.

If the waves are described by their wave vectors, with $\mathbf{k_i}$ being the incident and $\mathbf{k_o}$ the diffracted wave, then the vector relation between these two waves is (see Fig 4.2):

$$\mathbf{K} = \mathbf{k}_i - \mathbf{k}_o \tag{4.2}$$

Since the energy remains constant during the diffraction (the process is elastic), the lengths of the wave vectors are the same for waves before and after the diffraction:

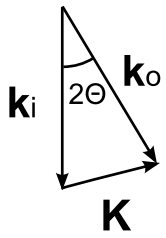

Figure 4.2: The wave vectors of incident ($\mathbf{k}_i$) and diffracted ($\mathbf{k}_i$) waves. The difference between them is **K**, and the angle is 2θ.

$$|\mathbf{k}_i| = |\mathbf{k}_o| = |\mathbf{k}| = \frac{2\pi}{\lambda} \tag{4.3}$$

By taking into account the geometric relation between these vectors from the Fig. 4.2, angle θ can be calculated as:

$$sin\theta = \frac{|\mathbf{K}|}{2|\mathbf{k}_i|} \tag{4.4}$$

By combining Eq. 4.1 with Eq. 4.2 and Eq. 4.4, the following expression for $|\mathbf{K}|$ can be obtained:

$$|\mathbf{K}| = \frac{2\pi}{d} \tag{4.5}$$

This equation is the diffraction condition and it states that the interference will be constructive if the difference between the wave vectors of the incident and diffracted waves is equal to the vector from the reciprocal lattice $|\mathbf{G}|$, where $|\mathbf{G}| = \frac{2\pi}{d}$ [Ref. 52].

Laue had interpreted Eq. 4.5 correctly in a vector form [Ref. 52].

$$\mathbf{k}_i - \mathbf{k}_o = \mathbf{G} \tag{4.6}$$

This theorem is more general because it does not require the assumptions used by Bragg, that reflection is mirror-like and from the parallel planes of atoms. The only assumption that is made is that scattering is elastic.

4.2 Ewald sphere

The Ewald sphere is a geometric construction that shows the relation between the wavelength of the incident and diffracted waves, the diffraction angle for a given reflection and the reciprocal lattice of the sample (Fig. 4.3)

The Ewald sphere has a radius of $r = \frac{2\pi}{\lambda} = |\mathbf{k}|$. If the Ewald sphere intersects with the point of the reciprocal lattice (colored grey in Fig 4.3), Laue condition is satisfied, thus giving the constructive interference of the diffracted waves. This is what is seen as the diffraction spot at the detector.

4.3 Effect of a thin film

In Fig 4.3 there are only a few discrete points where Laue condition is fulfilled. In the case of thin films, the translational symmetry of the three-dimensional crystal breaks down. The thin films have translational symmetry in two dimensions, but in the dimension normal to their surface this translation is limited. This causes the spots in the Ewald sphere to become elongated (Fig. 4.4) [Ref. 55].

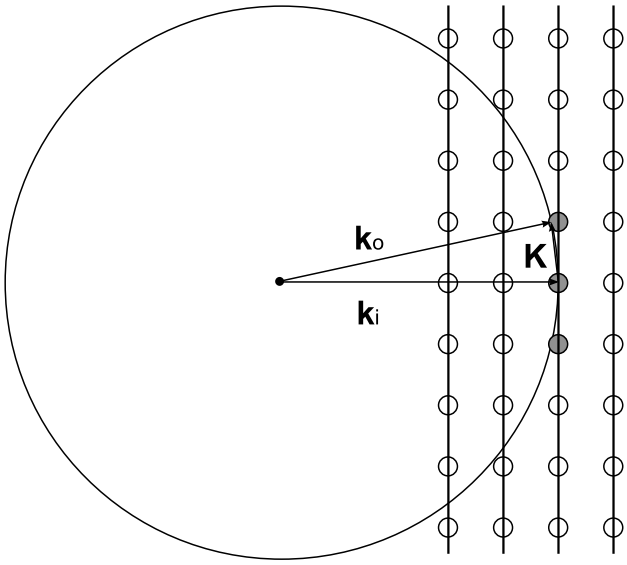

Figure 4.3: Ewald sphere. The grey spots depict the reciprocal lattice points for which Laue condition is fulfilled. $\mathbf{k_i}$ is the incident and $\mathbf{k_o}$ the diffracted wave.

In the case of only one layer of atoms (e.g. surface), the “spots“ would become ”rods“ [Ref. 56]. In the case of the Ewald sphere with elongated spots, the sphere will intersect with more of them than if the spots were not elongated. This leads to the higher number of diffraction spots for the diffractions of thin films than for the diffraction of bulk samples.

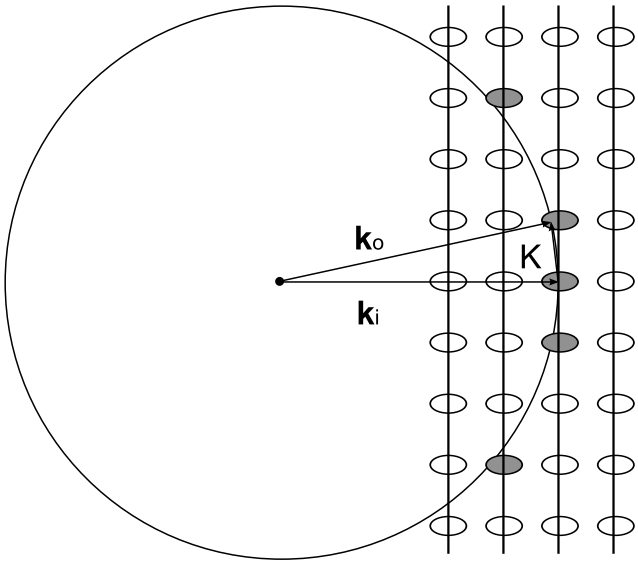

Figure 4.4: The effect of the thin film on the reciprocal lattice construction. Laue condition is fulfilled for more lattice points than in case of the bulk sample.

4.4 Structure factors

The amplitude of the Bragg peaks is proportional to the square of the structure factor, which is defined as:

$$S_{hkl} = \sum_j f_j \cdot e^{i\mathbf{G}\cdot\mathbf{r}_j} \tag{4.7}$$

Here, r_j is the postion of the atom j in the unit cell, f_j is the scattering power of the single atom, also known as atomic form factor, and **G** is the reciprocal lattice vector.

The structure factor is important because it describes the way in which the atoms of the crystal unit cell scatter the incident beam. It takes into account two things:

different atoms have different scattering power (f_j), and waves scattered from the atoms at the different positions in the unit cell will have a phase difference, ($\mathbf{G} \cdot \mathbf{r}_j$). It is important to emphasize that, due to the fact that different incident beams react with the matter through different processes, the atomic form factor also depends on the type of the incident beam, e.g. the atomic form factors for the X-rays' diffraction and for the electron diffraction differ by a few orders of magnitude.

4.5 Debye-Waller effect

The intensity of the diffracted electrons is:

$$I_{hkl} = |S_{hkl}|^2 = |\sum_j \sum_i f_j f_i \cdot e^{i\mathbf{G}\cdot(\mathbf{r}_j - \mathbf{r}_i)}|^2 \tag{4.8}$$

This equation is valid only if the atoms are 'frozen'. Debye [Ref. 57] and Waller [Ref. 58] found that due to the thermal motion of the atoms the intensity of the diffracted beam decreases with the crystal temperature. The peak intensity is lowered, but the profile of the diffracted beam remains the same (see Fig 4.5).

The Debye-Waller factor *DW(T)* quantifies this change in intensity:

$$DW\,(T) = \frac{I_T}{I_0} = e^{-\frac{1}{3}\langle \Delta \mathbf{r}^2 \rangle \mathbf{G}^2} \tag{4.9}$$

Here I_T is the intensity of the diffracted beam at the temperature *T*, I_0 is the intensity of the diffracted beam for the 'frozen lattice' and $\langle \Delta \mathbf{r}^2 \rangle$ is the mean square atomic displacement.

Eq. 4.9 shows that the reason for the Debye-Waller effect is the thermal

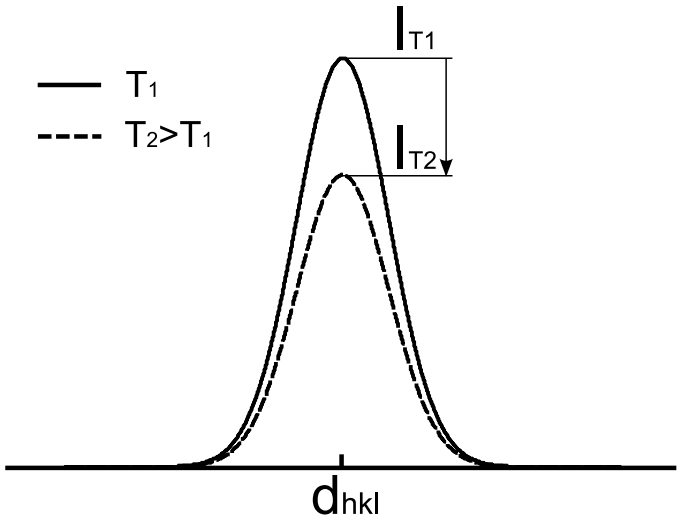

Figure 4.5: The Debye-Waller effect. The peak intensity decreases with the increase of the sample temperature, but the profile width remains the same.

vibrations of atoms near their equilibrium positions. If the lattice temperature increases, the mean square atomic displacement will also increase, the Debye-Waller factor will decrease and therefore, the intensity of the diffracted beam will decrease.

The calculation of the $\langle \Delta \mathbf{r}^2 \rangle$ can be done in analogy with the Debye theory of the specific heat [Ref. 59]. The Debye-Waller factor is [Ref. 60]:

$$DW\,(T) = exp\left(-\frac{6h^2T}{mk_B\Theta_D^2}\cdot\Phi(\frac{\Theta_D}{T})\cdot\frac{sin^2\Theta_B}{\lambda^2}\right) \tag{4.10}$$

Here Θ_D is the Debye temperature of the material, T is the temperature, m is the mass of the atom, k_B is the Boltzman's constant, $\Phi(\frac{\Theta_D}{T})$ is the Debye function, λ is the wavelength of the incident beam and Θ_B is the Bragg angle.

The Debye function can be approximated [Ref. 60]:

$$\Phi(\frac{\Theta_D}{T}) = \begin{cases} 1.642\frac{T}{\Theta_D} + \frac{\Theta_D}{4T}; & \frac{\Theta_D}{T} > 4.5 \\ 1 + (\frac{\Theta_D}{6T})^2 - \frac{1}{3600}(\frac{\Theta_D}{T})^4; & \frac{\Theta_D}{T} < 4.5 \end{cases} \tag{4.11}$$

Combining Eq. 4.1 with Eq. 4.10 gives:

$$DW\,(T) = exp\left(-\frac{6h^2T}{mk_B\Theta_D^2} \cdot \Phi(\frac{\Theta_D}{T}) \cdot \frac{1}{4d_{hkl}^2}\right) \tag{4.12}$$

Here d_{hkl} is the distance between the origin and the (hkl) plane.

It follows from Eq. 4.12 that the Debye-Waller effect is stronger for smaller d_{hkl}. Thus the decrease of the intensity of the diffracted beam will be more pronounced for diffraction of high order.

Chapter 5

Time resolved experiments

5.1 Experimental setup

As a change to the experimental setup described in Section 3.1, the output of the laser was divided into two beams (see Fig. 5.1). One beam was frequency-tripled as before and served for the production of the electron probe pulses as described in Chapter 3. The other was passed through the time-delay stage and used as a pump pulse for optical excitation of the sample.

This technique, known as a pump-probe technique, provides excellent synchronization between these two pulses, thus ensuring no time jitter between electron and laser pulses at the sample. By varying the time delay between the pump and the probe pulse, time-resolved measurements of processes induced in the sample by the pump pulse can be performed. For example, one can monitor the increase of the lattice temperature caused by the pump pulse by measuring the time-dependence of the Debye-Waller effect. In order for the probe pulse to detect the changes from a homogeneously excited portion of the sample, the

area of the pump beam should be sufficiently larger (5-10 times) than that of the probe beam.

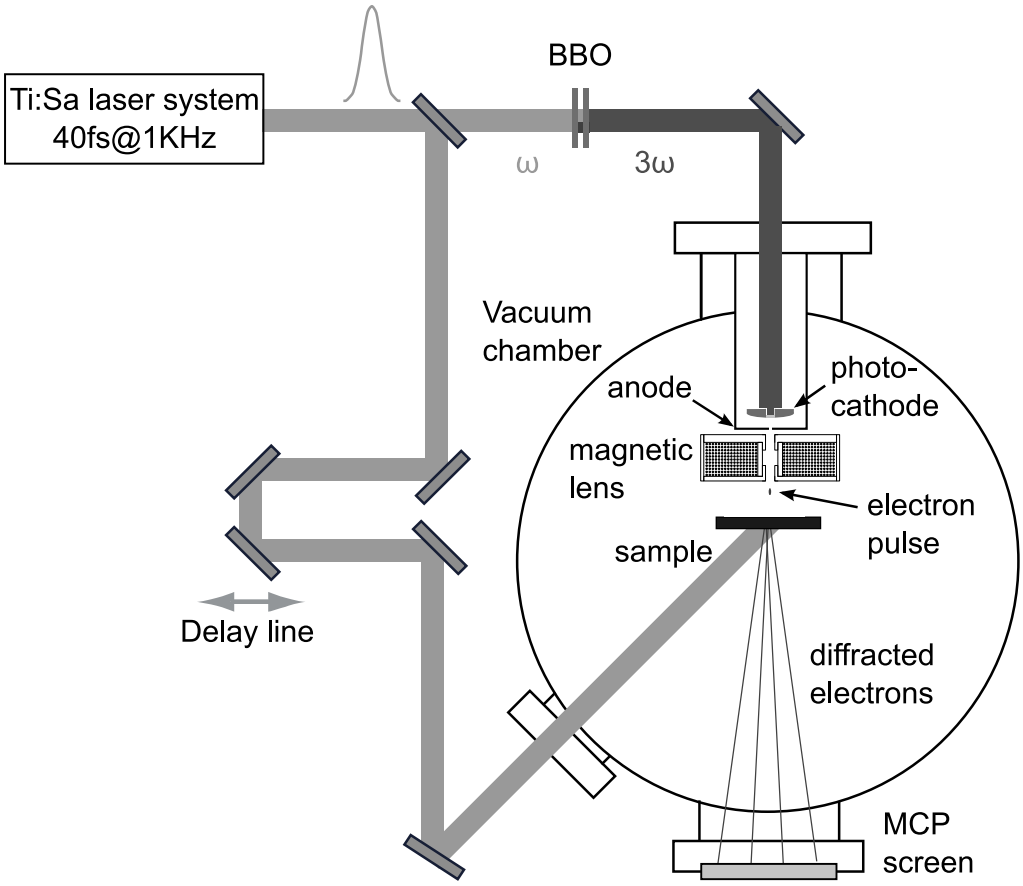

Figure 5.1: Experimental setup for pump-probe experiments. As an addition to the experimental setup already shown (Fig. 3.6), a beam splitter was put into the beam, and the reflected beam was sent to a delay stage and onto the sample as a pump.

There are two different geometries for realizing the pump-probe experiment: transmission and reflection. In a transmission pump-probe experiment, the probe beam is passed through the sample. The sample can be pumped from the same or from the opposite side. This kind of experiment requires a thin sample, otherwise

the probe signal would not be strong enough to be detectable after having passed the sample. In a reflection pump-probe experiment, both the pump and the probe beam arrive at the sample from the same side, and in this case, the reflected probe signal is recorded. With this geometry, bulk samples can be used.

For experiments that are discussed in this thesis, the transmission geometry with the pump and probe beam arriving from the opposite sides was used (see Fig. 5.2). The probe beam was normal to the sample plane, and the pump beam was at an angle of $\Theta = 45°$.

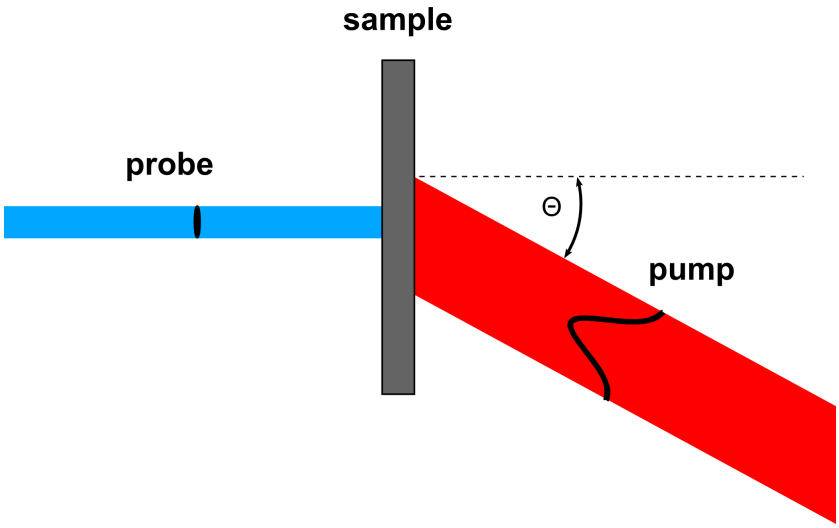

Figure 5.2: Pump probe experiment. The pump beam (red) arrives at the sample plane with angle Θ. The probe beam (blue) is normal to the sample plane.

5.2 Spatial overlap between the laser beam and the electron probe beam

Since the electron beam is not visible, it is not possible to determine the electron beam position at the sample by optical observation. For determining the position of the electrons beam, a special sample holder was constructed (Fig. 5.3). This

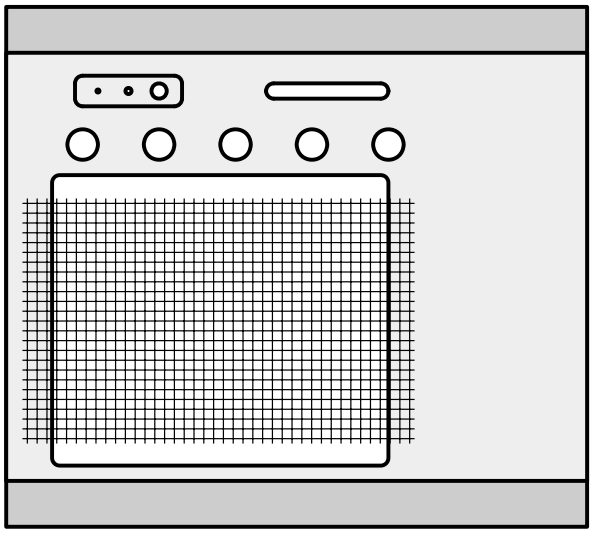

Figure 5.3: Sample holder. The top raw contains three holes with different diameters: 0.2 mm, 0,4 mm and 1 mm, and one long slit, 1 mm wide and 8 mm long. In the second row there are 5 holes, each 2 mm in diameter, for placing TEM grids. In the lower part there is a 19 mm $\times$ 22 mm hole for attaching mesh with thin films.

holder had holes of different shapes and sizes in order to simplify the positioning of the electron beam. In the first, top row, there were three circular holes with different diameters (0.2, 0.4 and 1 mm) and one long slit (8 mm$\times$1 mm). Using these, the position of the electron beam could be precisely found.

The sample was first positioned horizontally so that the horizontal center of the slit was approximately above the electron beam. At this point, the electron

beam was blocked. Then, the sample holder was slowly lowered until the electron beam again became visible on the MCP. In this way the vertical position of the electron beam was found.

The sample holder was then moved to the right, so that electrons would no longer pass through the slit, but through one of the circular holes. The best results were obtained when using the middle hole. The experimental setup was equipped with a CCD camera which was monitoring the sample holder position. Once the position of the electron beam was found, it was marked on the monitor.

Using the last mirror in front of the chamber, the pump beam was positioned at the same place as the electron probe beam. The CCD camera was monitoring this beam for any misalignments.

Also, it is important to notice that the size of the pump beam was $\sim$1 mm in diameter (FWHM), 5 times larger than the probe beam. This was essential to ensure that the sample was pumped uniformly over the whole surface we were probing.

5.3 Temporal overlap between the laser pump and the electron probe beams

For finding the temporal overlap between the pump and the probe beam, the spatial overlap had to be found first, using the technique described in Section 5.2.

A method similar to the one described in [Ref. 61, 62] was used to find the temporal overlap. The focused pump beam was used to extract photoelectrons

from the metal, and the part of the probe beam was deflected by this cloud of the photoelectrons. Either holes in the sample holder or a part of the mesh without the sample was used for making the photoelectrons.

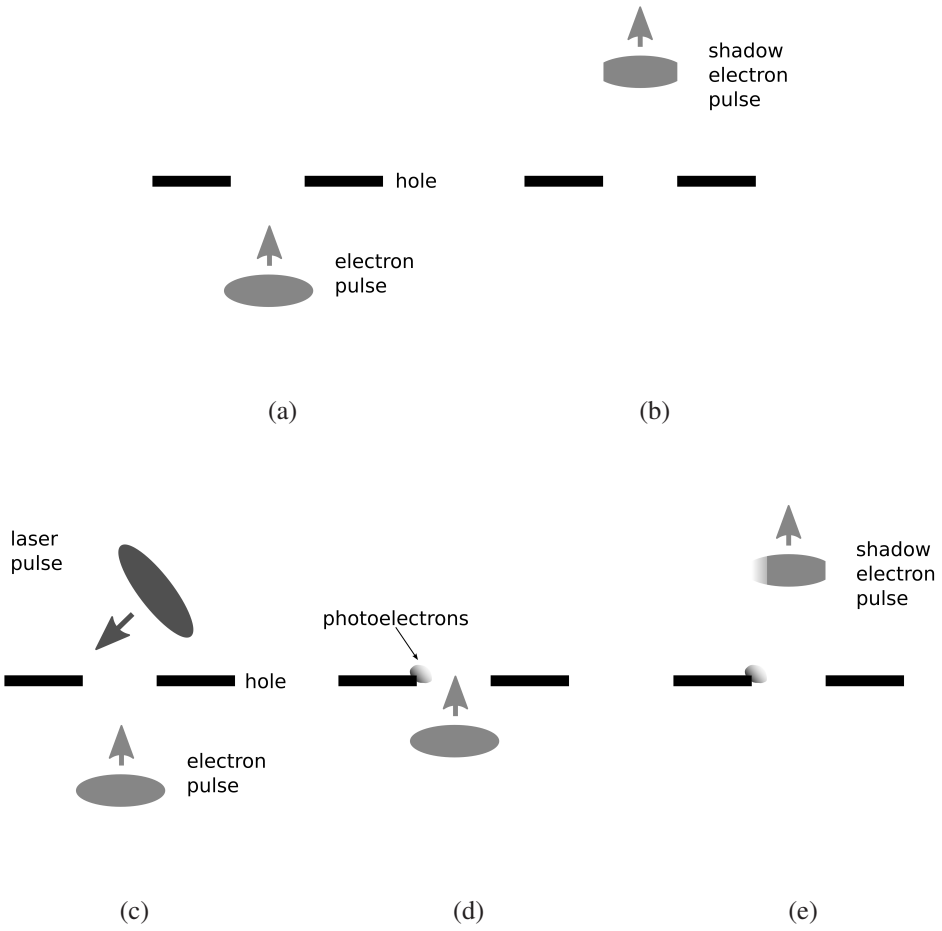

Figure 5.4: a-b) Formation of the electron shadow without the pump beam; c-e) Formation of the electron shadow with the pump beam arriving before the electrons

The electron beam was positioned in such a way that it passed through the 400 μm hole. This was done with an unfocused beam, so that only the central part of the beam was passing through, while the rest was blocked. The focused

pump beam was then positioned at one side of the hole, and it had a 150 μm diameter and an energy fluence of $\sim$10 mJ/cm^2. When the pump pulse hit the metal side of the hole, photoelectrons were emitted. If the electron pulse went through the hole before the pump pulse arrived, the electron spot at the MCP would be the shadow image of the hole. If, on the contrary, the pump pulse arrived first, the photoelectrons would deflect some of the electrons from the pulse, and the electron spot at the MCP would become distorted (see Fig. 5.4).

The change of the shadow image can be seen in Fig. 5.5.

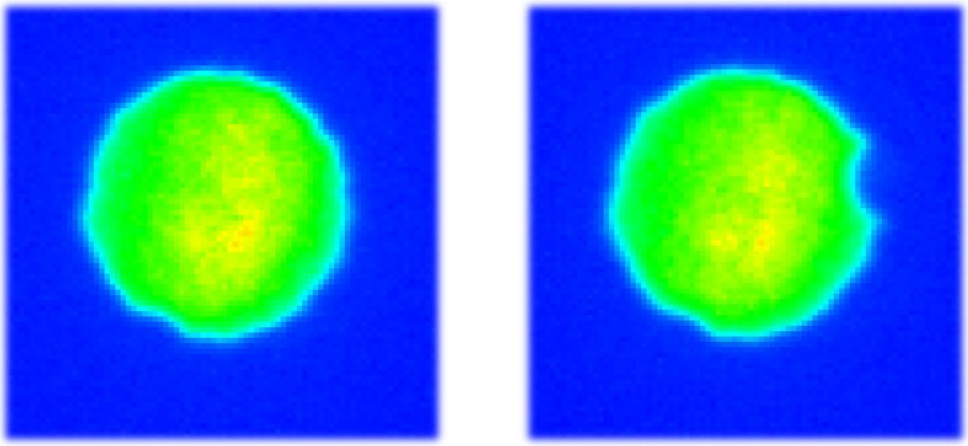

(a) a pump pulse arriving at the hole after a probe pulse

(b) a pump pulse arriving at the hole before a probe pulse

Figure 5.5: Time-zero measurement at the hole. The change of the shadow contour at the right image indicates that a pump pulse arrived at the hole before a probe pulse.

The right side of the hole shadow image in Fig. 5.5(b) had changed with respect to Fig. 5.5(a). This change could be quantified using the RMS (root mean square) value of the difference of a pixel intensity. For each pixel, the square of the difference in intensity between these two pictures was calculated, the values for all the pixels from the changed region were added up, and the

square root of the sum was taken. This procedure was done for different time delays between the probe and the pump pulses. Assuming that the probe beam had a Gaussian time profile, it was expected that the RMS value would have an error function profile. The measured data was fitted with an error function, and the result is presented in Fig. 5.6.

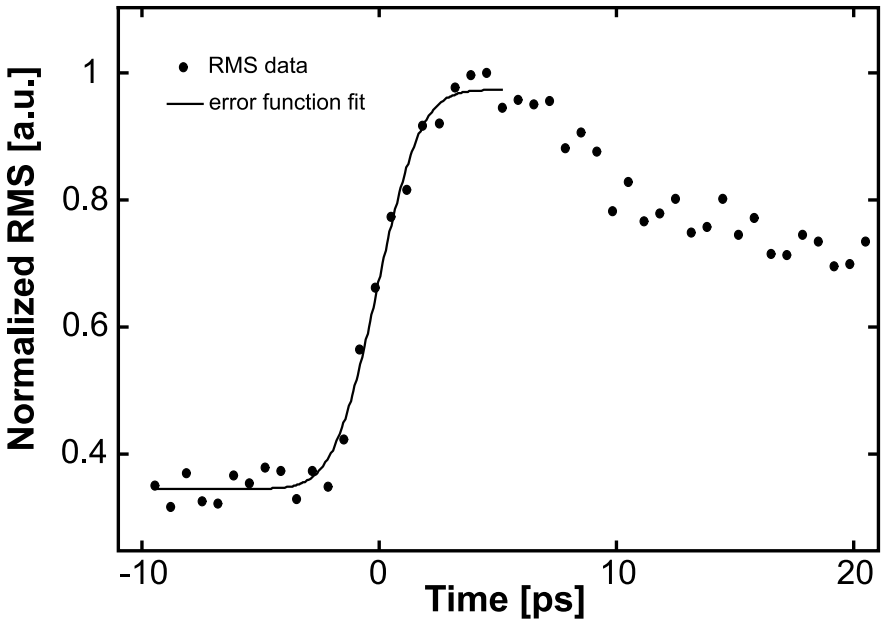

Figure 5.6: RMS value as a function of the time delay between the pump and the probe pulse.

A similar effect can be observed using a copper mesh instead of a hole (see Fig. 5.7). The mesh had a 15 μm thick wire with 200 wires/inch. In both cases, using the hole or the mesh, the rise time of the RMS value is $\approx$3ps. The time-zero measurement experiments were done with 5000-20000 electrons per pulse. It was expected that the RMS rise time depended on the numbers of electrons, but this was not the case. The explanation for this behavior is that photoelectrons were extracted from the metal by the three-photon absorption process, and they

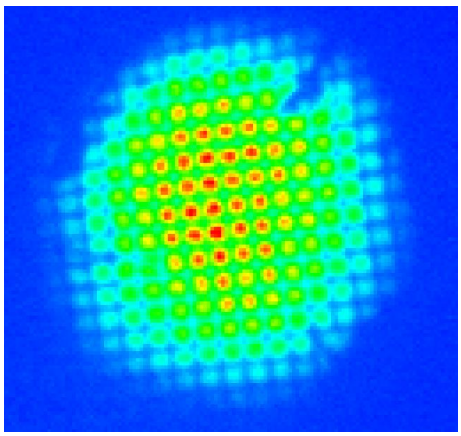

(a) a pump pulse arriving at the mesh after a probe pulse

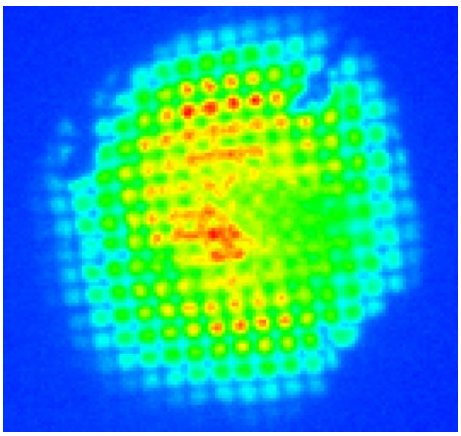

(b) a pump pulse arriving at the mesh before a probe pulse

Figure 5.7: Time zero at the mesh. As with the hole, the change in the shadow contour at the right picture indicates that a pump pulse arrived at the mesh before a probe pulse.

had low kinetic energy, in the range of a few hundreds of meV (work functions for copper and stainless steel are 4.7 and 4.1 eV, respectively, and the energy of the pump photons was 1.55 eV). These photoelectrons needed at least a few picoseconds to move far enough from the metal surface in order to affect the electrons in the probe pulse.

5.4 Temporal resolution

The temporal resolution of the electron diffraction experiments, apart of the duration of the electron probe pulse (τ_{el}), depends on several other factors. First, the duration of the pump pulse (τ_{las}) must be taken into account, together with the angular factor that results from two beams propagating with different velocities and different angles with respect to the sample ($d_{el} \cdot sin(\Theta)/c$), where d_{el} is the diameter of the electron beam (see Fig. 5.8).

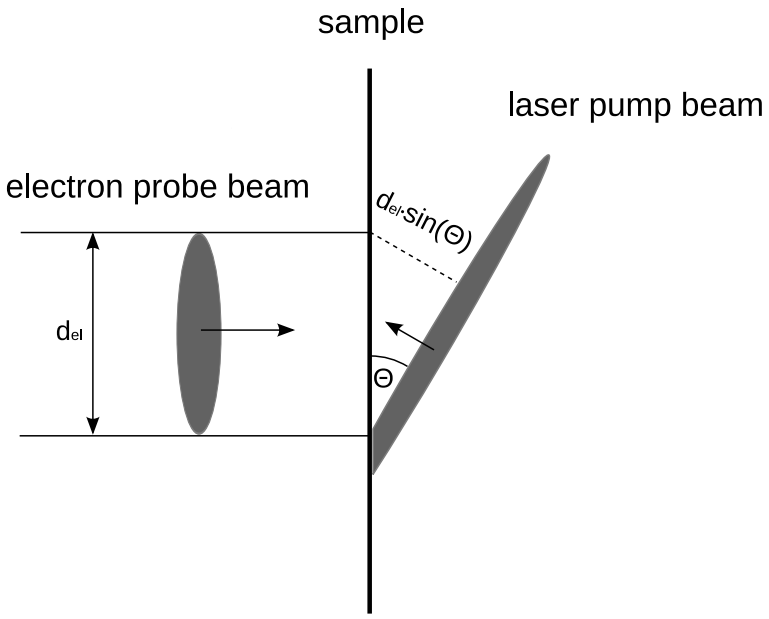

Figure 5.8: The pump and the probe beam arriving at the sample plane with different angles. The pump beam is arriving at the sample plane with angle Θ, which results in a path difference of $d_{el} \cdot sin(\Theta)$.

Next, there is the contribution from the finite thickness of the sample (τ_s). Given that the pump and the probe beam are counterpropagating through the sample, the probe beam will experience the pump-induced change with a different time-delay at a different sample depth. However, sample thickness usually plays an important role in the pump-probe experiments with gas-jets, where the thickness of the sample is in a 10-100 μm range [Ref. 17, 63]. In the case of experiments with solid thin samples, with a thickness of a few tens of nm, this contribution is negligible in comparison with the electron pulse duration [Ref. 32].

Another factor comes from the fluctuations of the high voltage supply used for electrons acceleration (τ_{hvs}). If the accelerating voltage would differ for two pulses, the time necessary for them to arrive at the sample would also differ, and this would result in a jitter between the pump and the probe beam. The stability

of the high voltage supply used in this experimental setup was 0.01%, so this term can be neglected [Ref. 32].

The final temporal resolution of the experiment is then the convolution of these factors.

$$\tau_{exp}^2 = \tau_{el}^2 + (\tau_{las} + \frac{d_{el}}{c} \cdot sin(\Theta))^2 \tag{5.1}$$

The duration of the electron pulses was previously discussed in Chapter 2, and it was estimated that, for 2500 electrons per pulse, this value was τ_{el}=650 fs. The temporal resolution of the experimental setup would then be 800 fs, for 200 μm electron pulse diameter and 45° angle between the pump and the probe beam.

An additional contribution to the time resolution with thin film samples could come from the sample holder movement precision, but only in the case of the destructive measurements. In this case, the sample would have to move between single shots in order to have a new spot on the sample for experiment. If the sample is not moving in its own plane, the new spot would not be at the same position as the old one, so the timing of the pump and the probe pulse would be different.

5.5 Sample preparation

Thin free-standing samples are necessary for performing electron diffraction experiments in transmission geometry. In order to achieve sufficient signal-to-noise ratio of the diffracted signal in the presence of some background signal

probably being due to inelastically or multiple scattered electrons, the sample thickness had to be limited.

The samples used in the experiments were 22 $\pm$ 2 nm thick free-standing bismuth films. They were made by evaporating bismuth onto polished NaCl crystals. After the bismuth film was deposited on the crystal, it had to be detached from the substrate and transfered to the mesh. This was done by floating off the bismuth film from the NaCl crystal by slowly inserting the crystal into the container filled with distilled water. The bismuth film detached from the crystal and stayed on the surface of the water. Then, by positioning the sample holder under the bismuth film and slowly lifting it, the bismuth film was 'fished out' onto the mesh. After waiting a few hours for the sample holder to dry, the sample was ready to be inserted into the chamber.

The quality of the thin bismuth film was checked using transmission electron microscopy (TEM). The TEM image can be seen in Fig 5.9.

The TEM image consists of well-defined diffraction spots, which indicates that the sample was crystalline. Bismuth has a 6-fold symmetry, but the diffraction patterns had 12-fold symmetry. This observation can be explained by the presence of two bismuth domains which are rotated for 90°with respect to the vertical axis. All the diffraction spots correspond to Miller indices (hkl) with l=0. Thus the bismuth was epitaxially grown in the *(001)* direction (the *(hkl)* indices are in hexagonal notation).

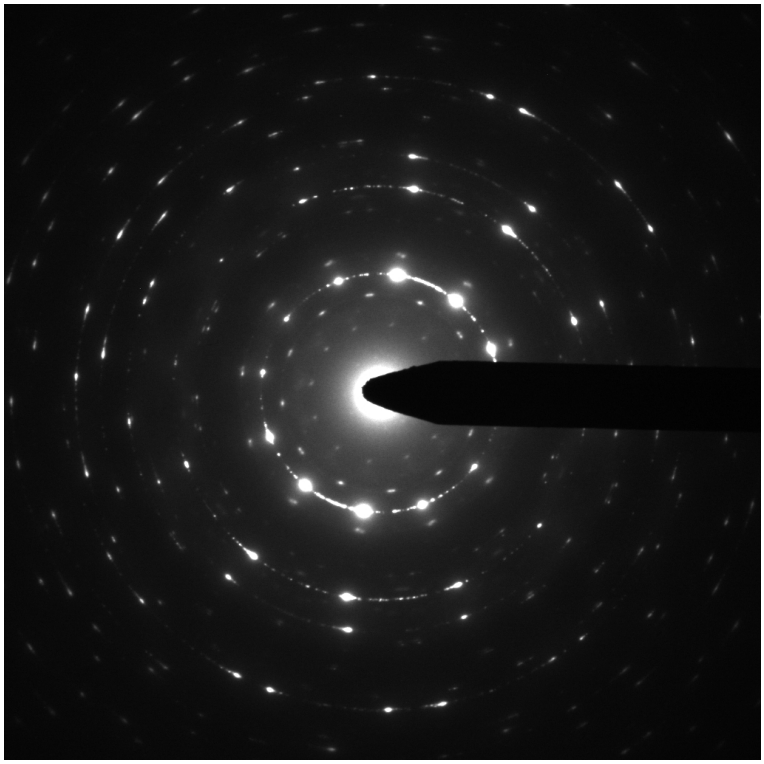

Figure 5.9: The TEM image of the bismuth thin film.

5.6 Stability of the electron source

The pump-induced changes in the intensity of the diffracted signal observed in the experiments described in this work are in the order of few percent. The stability of the electron current of the source is therefore an important requirement. The accuracy needed for these experiments is in the 1% range.

The experimental setup was positioned approximately 5 meters away from the laser system. The laser beam (800 nm) traveled from the laser system to the experimental setup through pipes to minimize the effects of the fluctuations of the air temperature and density. Inside the experimental setup, both beams (800 and 267 nm) traveled through pipes. This was extremely important especially for

the 267 nm beam, because small changes in the air temperature or the air movement caused by the air conditioning system could change the beam properties significantly.

5.6.1 Short-term stability

The energy of the laser beams was measured at two points in the setup by photo diodes. The photo-diodes were positioned:

- before the entrance of the chamber, monitoring the 800 nm beam (pump)

- before the entrance of the chamber, monitoring the 267 nm beam (probe)

For the 267 nm beam, not only the energy but also the position stability played a significant role in the overall stability of the electron source. When the 267 nm beam hit the photocathode, electrons were emitted from the area illuminated by the beam, 1mm in diameter. Out of this bunch, only the electrons positioned in the central 100 μm of the photocatode passed through the pinhole. If the 267 nm beam moved, the electrons which pass through the pinhole would be produced by a different part of the beam, and their number could differ. To measure the influence of the positioning stability of the 267 nm beam on the stability of the electron source, a 200 μm pinhole was positioned in front of the photodiode which was measuring the energy of the 267 nm beam.

In Figure 5.10 the stability data for these two beams are plotted.

The energy of a single pulse was measured over 1000 pulses. The stability was quantified by the standard deviation (σ), which measures the spread of data about the mean value [Ref. 64], $\sigma = \sqrt{\frac{1}{N}\sum_{i=1}^{N}(x_i - \overline{x})^2}$.

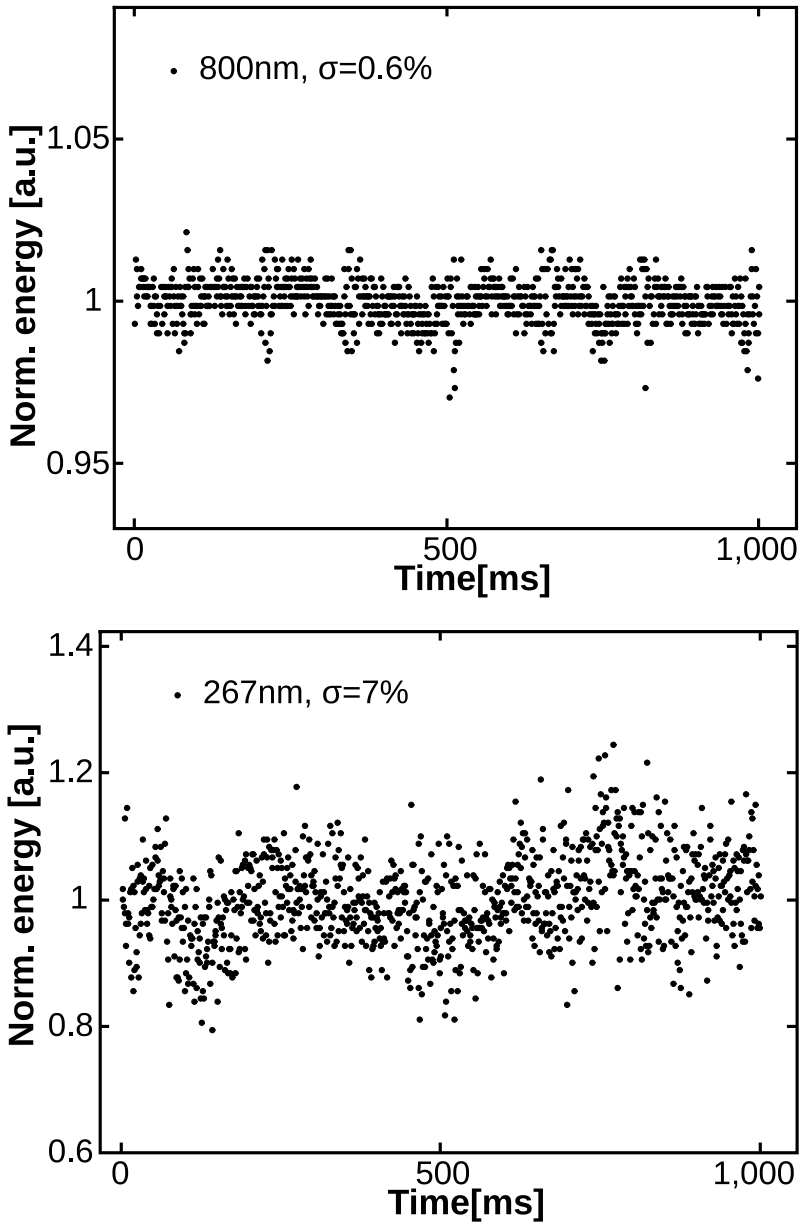

Figure 5.10: The energy of the 800 nm beam and the 267 nm beam through the pinhole. The energy was measured over 1000 pulses. The standard deviation for the 800 nm beam was 0.6%, and for the 267 nm beam it was 7%

Since the energy of the third harmonic beam is proportional to the third power of the energy of the fundamental beam ($E_{3rd} \sim E_{fun}^3$), it was expected that the

standard deviation of the third harmonic beam would be three times bigger than that for the fundamental beam. In this case, it was more than three times larger than the expected value. This would imply that the position stability of the third harmonic was not sufficient to achieve better electron yield stability. One way of minimizing the effect of the position instability of the 267 nm beam was to focus the beam onto the photocathode. This was done by the lens with 500 mm focal length. The stability of the focused 267 nm beam together with the stability of the 800 nm beam are presented in Fig. 5.11.

The energy of a single pulse was measured over 1000 pulses. The standard deviation of the pulse energy of the 267 nm beam when using the focusing lens was 2.9%, which is more then 4 times better than without the lens.

The next step was to measure the stability of the electron current of the electron source. This was accomplished by recording the MCP signal with the CCD camera and then integrating the CCD signal corresponding to the electron spot. The data for the single pulse intensity stability, 10 pulses average and 100 pulses average is presented in the Fig. 5.12.

The fluctuations of the electron signal depended on the fluctuations of the third harmonic laser energy (Fig. 5.11) and on the distribution of the signal intensity produced by one electron on the MCP screen (Fig. 3.15). For electron pulses which contain a few thousands of electrons, the fluctuation due to the different MCP signal produced by individual electrons can be neglected, and the expected fluctuation should be comparable to the fluctuation of the energy of the third harmonic laser beam.

The standard deviation depends inversely on the square root of the number of the electron pulses averaged in one data point. For the signal pulse, the standard

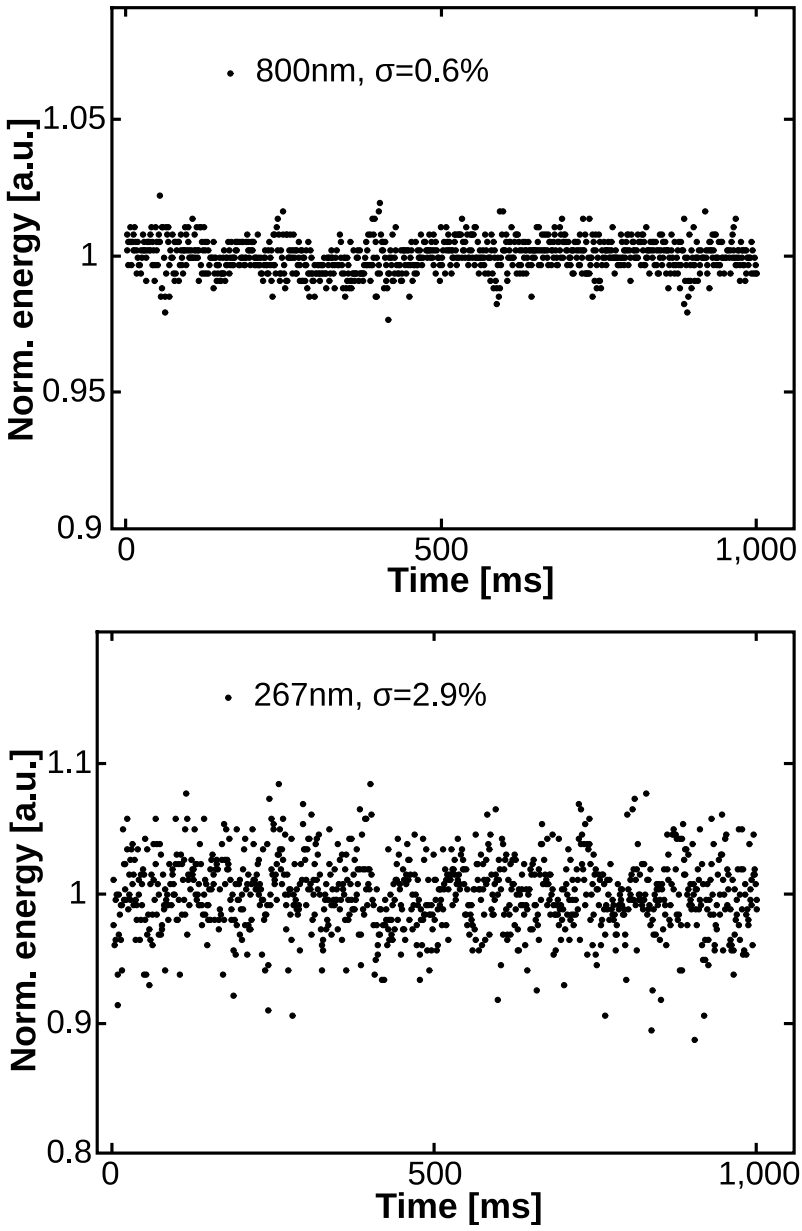

Figure 5.11: The energy of the 800 nm and the focused 267 nm beams. The stability was measured for 1000 shots. The standard deviation for the 800 nm beam was 0.6%, and for the 267 nm beam was 2.9%

deviation was 13%. For the 10 pulses average, the standard deviation was 3%, which was in agreement with the $\sqrt{N}$ dependence. For the 100 pulses average,

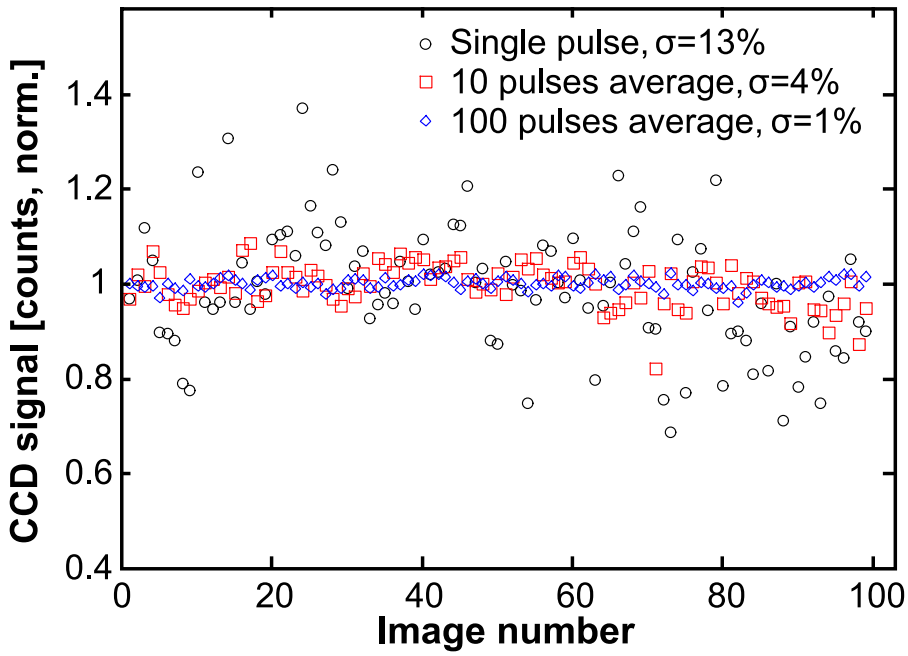

Figure 5.12: The stability of the electron spot intensity on the MCP for a single pulse, 10 pulses average and 100 pulses average. The standard deviation decreases with the square root of the number of averages.

the standard deviation becomes even smaller, only 1%.

Up to this value, the standard deviation depended on the number of averaged pulses as $\sigma \sim N^{-\frac{1}{2}}$. However, 1% was the minimal value for the standard deviation for this setup; if a higher number of pulses was averaged, the value did not become smaller.

The reason for not obtaining a stability better than 1% were the changes in the laser beam energy which occurred on a time scale comparable to the the acquisition time of one picture, so they could not be averaged out.

5.6.2 Long-term stability

The time required for one non-destructive, time-resolved measurement under the experimental conditions mentioned in this thesis was between 30 minutes to a few hours, depending on conditions, such as the number of electrons per shot, the voltage on the MCP plate, the type and the thickness of the sample etc. The measured electron signal should have a stability of 1% or better, in order to be able to observer small changes in the diffracted intensity. During the measurement time, the pulse energy of the laser beam could change. If this change was only 1%, the third harmonic energy would change by at least 3%, so the number of electrons per pulse would also change by at least 3%.

The intensity of the electron spot at the MCP was recorded during 25 minutes, and the result is presented in Figure 5.13.

As shown in this figure, the intensity of the electron spot at the MCP can change as much as 10% in a 20 minutes period. During this time the laser pulse energy of the 800 nm beam changed by 2%. This is much more than the precision needed for the experiments.

One of the ways to compensate for this intensity change was to introduce a repetitive-scanning technique. With this technique, only one picture of 500 ms - 2 s was acquired at each time-delay, so the whole time-scan was finished in a few minutes for 100 time points. This time-scan was then repeated and the signal for each time point was averaged until the averaged signal stability was satisfactory.

If the repetitive-scanning technique was not used, the time difference between taking the first and the last picture in the scan could be as much as two hours, and the laser parameters could change significantly during this period of

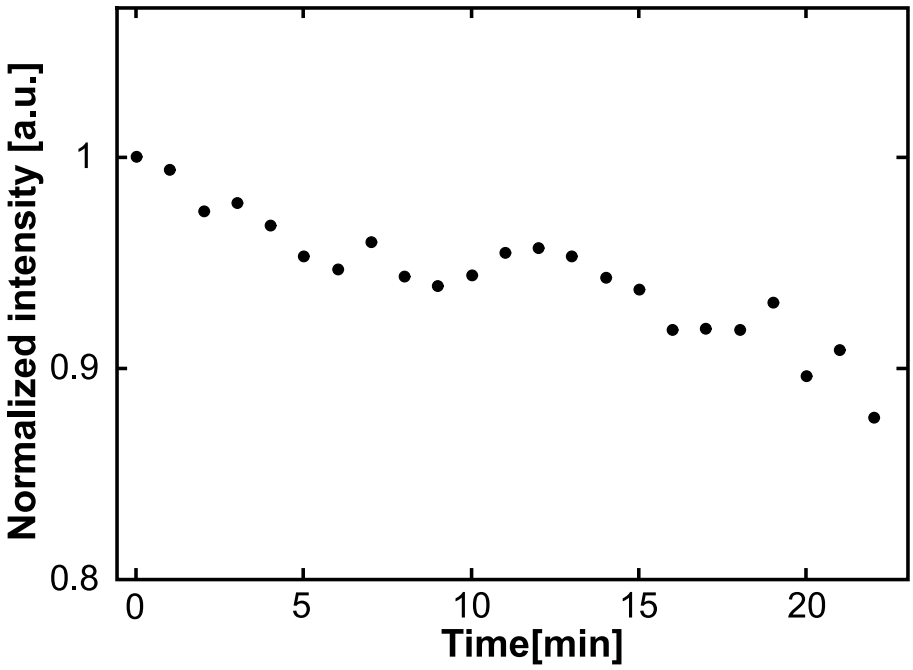

Figure 5.13: The stability of the intensity of the electron spot at the MCP during 25 minutes. Each picture was the average of 100 pictures with 3 ms exposure, therefore each point represents 300 pulses.

time. With the repetitive-scanning technique, in each scan the time difference between the first and the last picture taken was a maximum of 2 minutes, and all the changes in the laser energy that occurred in this time order were averaged over consequent scans. In this way it was possible to keep the stability of the electron intensity in the range of 1%.

5.7 Time resolved measurements

With this experimental setup, it was possible to measure the ultrafast response of thin films samples after optical excitation.

The material to be used as a sample was bismuth. Due to its low Debye tem-

perature (112 K, see App. B), the Debye-Waller effect is very pronounced, and the change in the diffracted intensity can be easily detectable. Ultrafast RHEED experiments have already been performed on bismuth [Ref. 25], but the temporal resolution was limited to 25 ps or more, due to the velocity mismatch of the pump and the probe beam at the sample. Now, it would be possible to improve temporal resolution to 1 ps or better.

The laser pulse used for pumping had a fluence of up to 1.5 mJ/cm^2 and a FWHM of 1 mm. Higher fluences led to irreversible damage to the thin film sample, which was manifested by a decrease of the diffracted and an increase of the non-diffracted signal intensity.
A static electron diffraction picture made by the ultrafast electron source is presented in the Figure 5.14.

This picture was acquired with a large number of electrons (20-30 million), so even the higher order of diffraction can be seen easily.

The central ring (1, see Fig. 5.14) of the group of three rings closest to the non-diffracted beam was the (110)-equivalent diffraction, where (110)-equivalent includes all the spots with the same lattice parameter d_{hkl} as the (110) spot ((110), (2$\bar{1}$0), (1$\bar{2}$0), ($\bar{1}\bar{1}$0), ($\bar{2}$10) and ($\bar{1}$20)). The two rings surrounding (110)-equivalent ring could not be identified as a bismuth diffraction, and they were found to be the diffraction signal from the remains of the NaCl crystals which were on the bismuth surface. These two rings were (200)-equivalent and (220)-equivalent diffractions from NaCl. The next two rings (2 and 3) came from the (300)-equivalent and (220)-equivalent diffraction. Ring (4), the 24 spots pattern, was the (410)-equivalent diffraction. After this, the (330)-equivalent and the

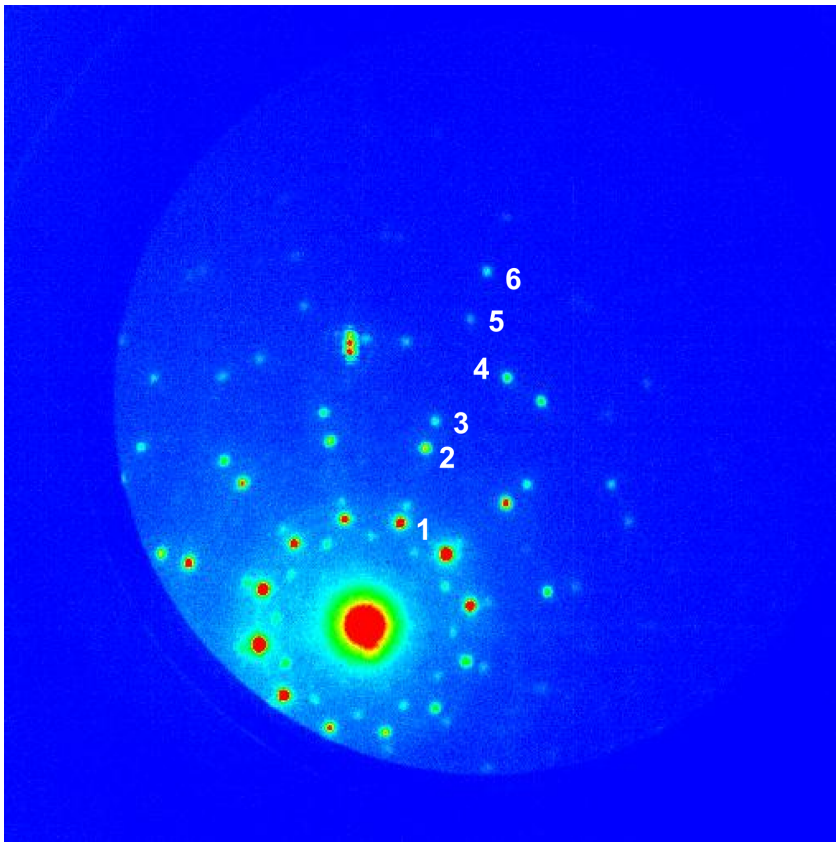

Figure 5.14: A static diffraction picture of the thin bismuth sample.

(600)-equivalent diffraction rings could be seen (5 and 6).

The diffraction orders that could be observed and the corresponding lattice constants for bismuth are presented in Table 5.7.

No.	hkl	d_{hkl} [Å]
1	110	2.28
2	300	1.32
3	220	1.15
4	410	0.87
5	330	0.77
6	600	0.66

Table 5.1: The diffraction orders and the lattice constants for bismuth

The most intense peak on the picture was the non-diffracted beam, and it is the limiting factor for the duration of the exposure for each picture. The intensity of the non-diffracted beam was almost two orders of magnitude larger than the intensity of the first diffraction ring. In order to obtain data for both the diffracted and non-diffracted signal, the CCD-recorded signal of the non-diffracted beam was attenuated. This was achieved by two pieces of a polarization foil taped one above the other onto the MCP screen on the position of the non-diffracted beam. The transmission of these two pieces of the polarization foil was measured, and it was 2%. With an attenuated CCD signal of the non-diffracted beam, the maximal signal on the CCD camera was one from the most intense diffraction spots, and the measurements were done in such a way that this value was kept at 70-80% of the CCD camera dynamic range.

The pump was then sent to the sample and, by using the previously explained repetitive-scanning technique. At each time point a picture with 500 ms exposition was taken and each time point was averaged 20 times.

Chapter 6

Results and Discussion

6.1 Data analysis

A measurement was performed with a 800 nm laser pump fluence of 1mJ/cm^2. The pump spot on the sample had a vertical and horizontal FWHM of 11 mm and 9 mm. The number of electrons per pulse in the probe beam was 2500. The sample was at ambient temperature, 18 °C.

The intensity of each of the diffraction spots in the diffraction image had to be measured. The main problem was to separate the diffracted beam signal from the background signal. The background signal consisted of the inelastically scattered electrons, multiple scattered electrons and the pump induced signal.

First, the rectangular region of interest was defined, with one diffraction spot in the center. The signal was then integrated in one dimension, resulting in a line profile. The line profile was fitted with a sum of the Lorentz function and a linear function, corresponding to the diffracted signal and the background, respectively.

The procedure was repeated for all diffraction spots, and the intensity of the

spots belonging to the same diffraction ring was summed.

An example of the integrated signal and the fitted function can be seen in Fig. 6.1.

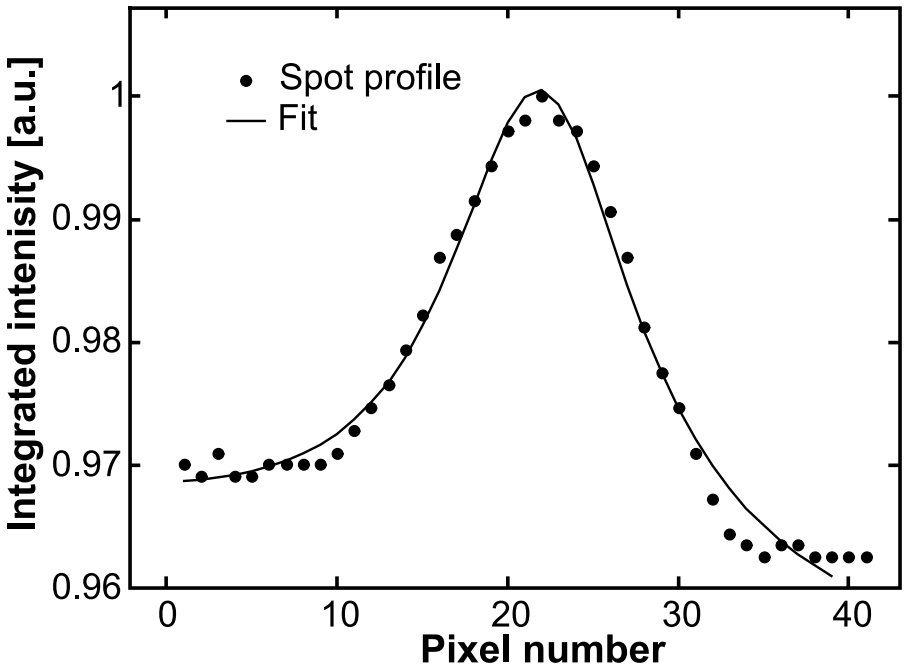

Figure 6.1: A fit of the intensity of one diffraction spot. The fitting function was the sum of a Lorentz function and a linear function.

After the fitting, two parameters were important: the height and width of the Lorentz peak. As expected, the width of the peak remained constant during the experiment, and the height of the peak changed. The change in the intensity of the diffracted spots for three different diffraction orders is presented in Fig. 6.2.

The data in Fig. 6.2 was fitted using two exponential decay functions:

$$I = \begin{cases} I_0 & , t < t_0 \\ I_0 - a \cdot (1 - e^{\frac{-(t-t_0)}{\tau_1}}) - b \cdot (1 - e^{\frac{-(t-t_0)}{\tau_2}}) & , t \geq t_0 \end{cases} \tag{6.1}$$

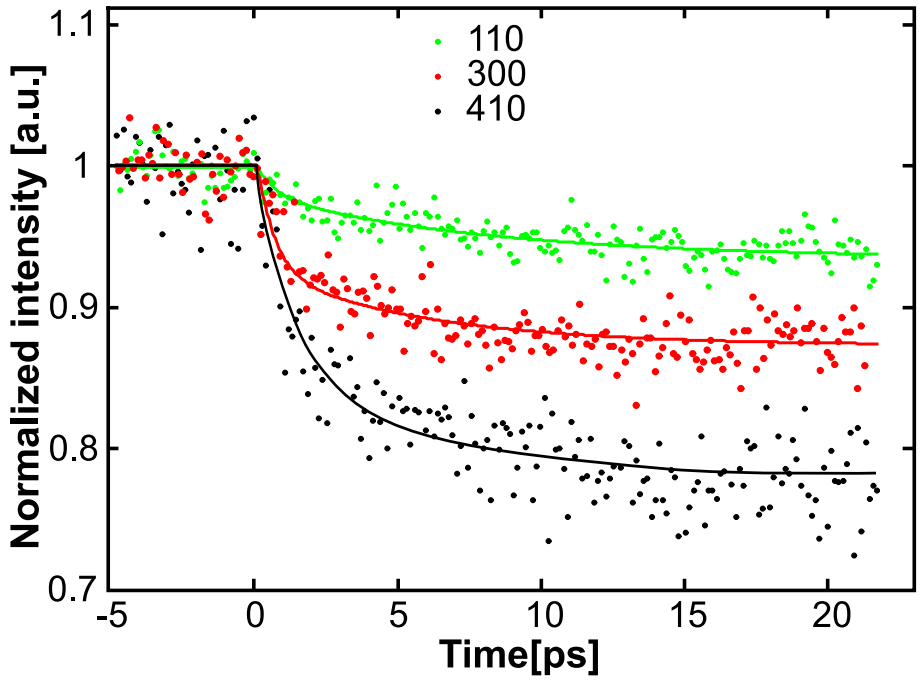

Figure 6.2: The intensity drop of the diffraction spots after the fast optical excitation of the bismuth sample. The pump fluence was 1mJ/cm^2

The results of the fitting are presented in Table 6.1. Since the data was previously normalized, the value for I_0 is 1 for all the spots.

hkl	a [%]	τ_1 [ps]	b [%]	τ_2 [ps]
110	2.1	.71	4.1	7.5
300	6.0	.63	8.4	4.8
410	1.0	.68	1.3	5.8

Table 6.1: Results of fitting the diffraction spots intensity change with two exponential decay functions.

All spots show the same behavior: there is a fast (τ_1 = 700 $\pm$ 400 fs) initial drop of intensity, followed by a slower drop ($\tau_2 \sim 6 \pm 3$ ps). The amplitude of the first drop is smaller that the amplitude of the second drop for all diffraction orders.

The ultrafast time-resolved experiments performed on bismuth [Ref. 65–71] were focused on observing the inner-cell dynamics, i.e. the fully symmetric coherent optical phonon A_{1g} . The bismuth diffraction spots sensitive to this optical phonon have Miller index $l \neq 0$; for even l the diffracted signal intensity should increase, and for odd l the intensity should decrease. Since all of the diffraction spots in this experiments have $l = 0$, the influence of the optical phonon on the diffraction intensity cannot be seen.

The fast drop observed in this measurement could be described by the decay of the optical phonon A_{1g} into the acoustic phonons. As has already been experimentally measured [Ref. 69], due to the fast dephasing time of the coherent optical phonon (1.17ps), the energy transfer of the optical phonon into the acoustic phonons is a faster process than the lattice heating by the excited carriers. Another work [Ref. 65] has measured the period of the lowest frequency of the A_{1g} phonon to have a vibrational period of 470 fs. This indicates that the energy transfer from the A_{1g} phonon to the acoustic phonons occurs on a timescale of one vibrational period.

The slower drop in the diffracted intensity can then be explained as an energy transfer from the excited electrons directly to the lattice, i.e. electron-phonon relaxation.

Another explanation for the two-drops behavior can be that the faster drop was caused by the electron-phonon relaxation and that the delayed Auger heating was responsible for the slower drop. The deleyed Auger heating was already observed in semiconductors, i.e. in silicon [Ref. 72], and it was shown that thin bismuth films can have semiconductor properties [Ref. 73–76]. The electron-

hole recombination time in bismuth was also measured, but only at low temperatures [Ref. 77].

The measured data also show that the temporal resolution of this experimental setup is better than 700 fs, which is even better than previously estimated in Chapter 5.

In Figure 6.3, the change of only one spot intensity (410) is plotted, and the regions for the two different drops are marked.

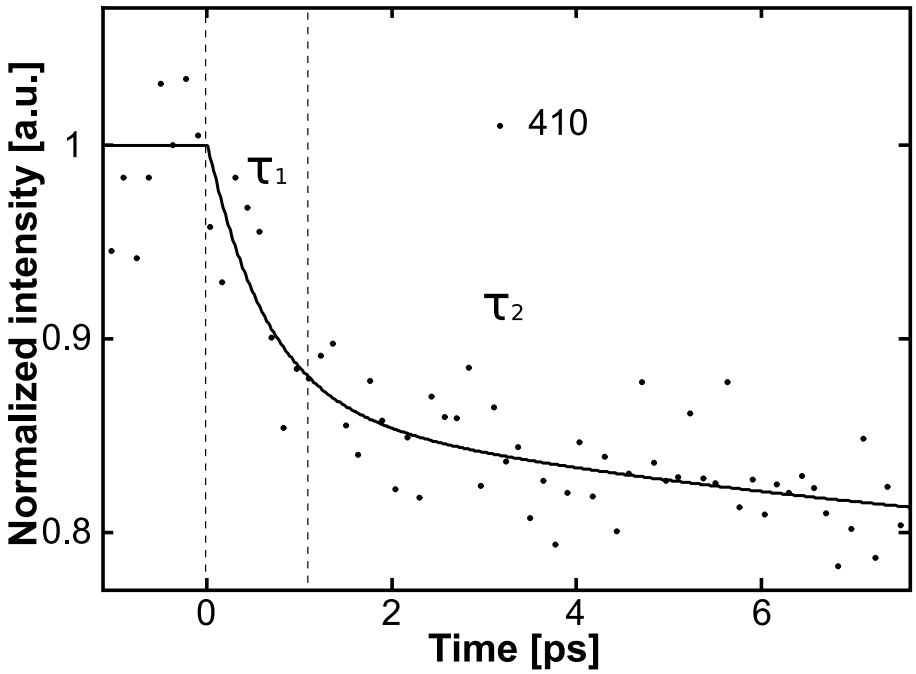

Figure 6.3: The intensity drop of the (410) diffraction spot. Two regions with different drop-time constants can be distinguished.

At this point, it would also be interesting to look at the importance of the number of electrons per pulse for the temporal resolution of the experimental setup. The measurement was repeated with a higher number of electrons per pulse (20000 e/pulse), and all the other parameters were kept the same. The

influence of the number of electrons per pulse on the temporal resolution is presented in Fig. 6.4.

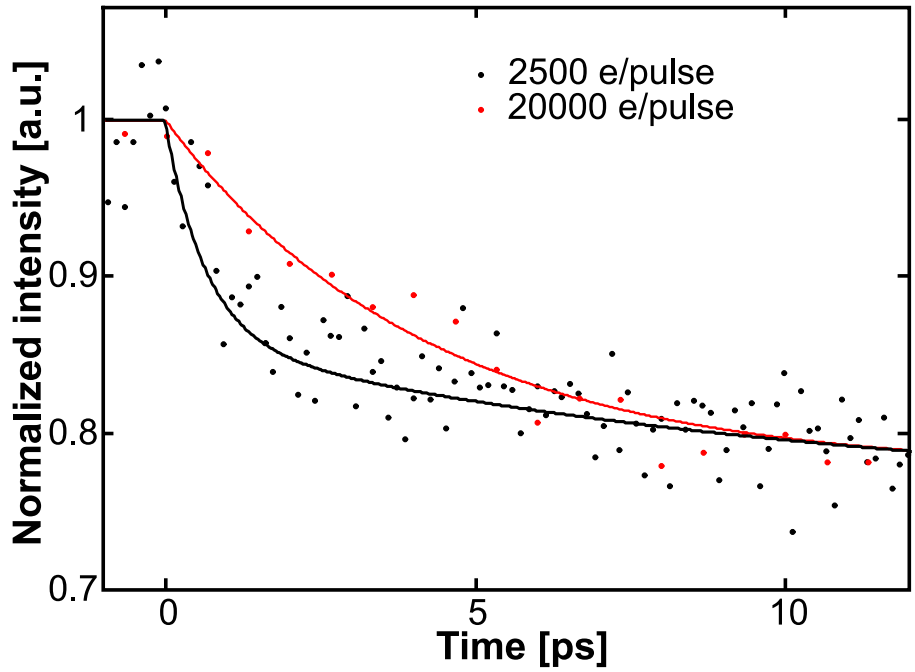

Figure 6.4: The effect of the number of electrons on the temporal resolution. With a higher number of electrons, it was impossible to observe the first drop.

With a higher number of electrons, it is impossible to distinguish between the two different time constants, and the intensity drop can be described with only one exponential function with a time constant of $\sim$4 ps. Here it is obvious that, in order to achieve sub picosecond temporal resolution, the number of electrons per pulse has to be kept at a few thousands.

As a result of the Debye-Waller effect, the intensity drop is dependent on the lattice constant (see Eq. 4.12) in following way:

$$-\,ln(\frac{I}{I_0}) = K \cdot d_{hkl}^{-2} \tag{6.2}$$

Here, K is a constant which depends on the material properties and the temperature of the material.

The graph showing the linear dependence of the $-ln(\frac{I}{I_0})$ on the d_{hkl}^{-2} is plotted in Fig. 6.5.

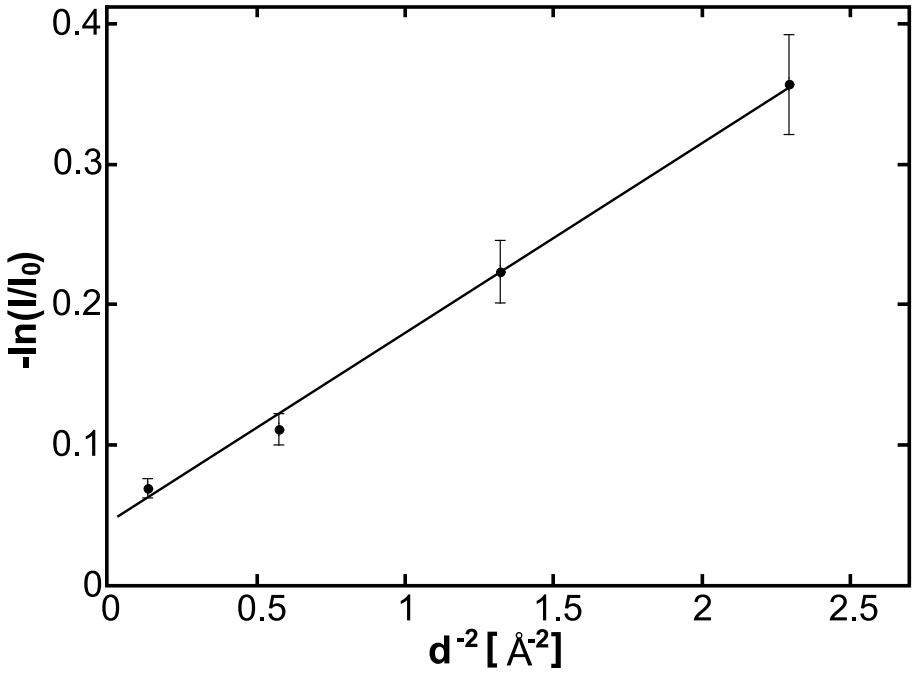

Figure 6.5: Debye-Waller factor value for different diffraction orders.

The coefficient K was calculated by a linear fit of the data, and it was found to be (0.14 $\pm$ 0.01) Å^2. Using this coefficient and Eq. 4.12, it was possible to calculate the temperature of the sample, which was 420 K. The graph does not start from 0, as expected, but cuts the y-axis at the value 0.04, which coresponds to the intensity drop of 4%.

The temperature of the sample could also be estimated by using the total energy

deposited in the sample and the specific heat capacity of the bismuth.

$$\Delta T = \frac{E}{c_p \cdot m} \tag{6.3}$$

Here, ΔT is the increase in temperature, E is the amount of the energy deposited into the sample, c_p is the specific heat capacity of the bismuth and m is the molar mass of the bismuth. Using this equation and the properties of the bulk bismuth (see App. B), the temperature rise of the sample was calculated to be ΔT=110 K, which gives 400 K for the temperature of the sample.

The measurement was repeated for a higher pump fluence, 1.5mJ/cm^2. Here, the drop of the diffraction peaks was larger. The graph showing the data for both fluences is shown in Fig. 6.6

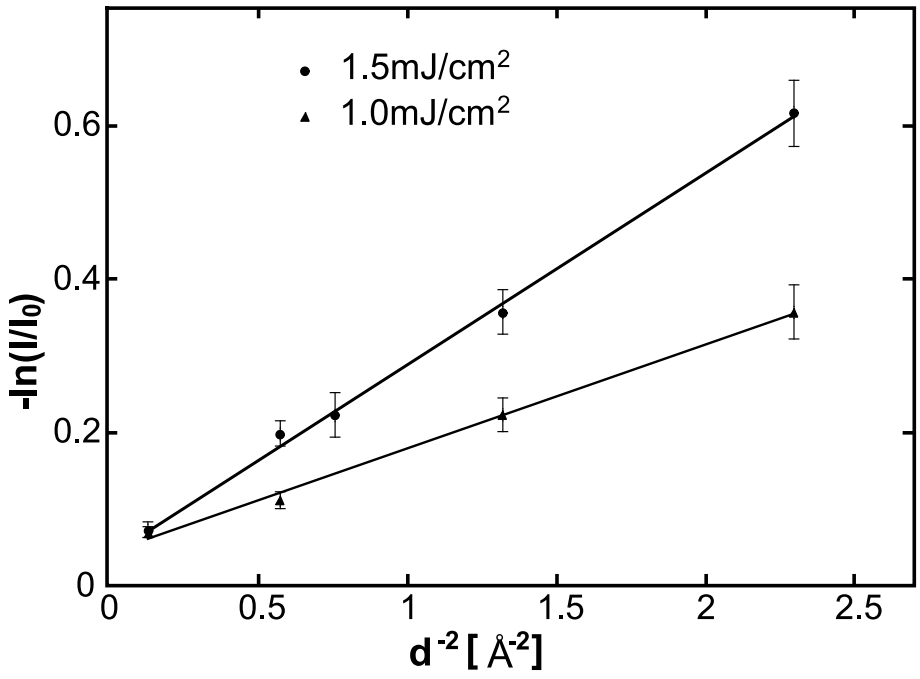

Figure 6.6: Debye-Waller factor for different diffraction orders and two different pump pulse fluences.

Using the coefficient of the fitted line, the temperature of the sample was calculated to be 510 K, while using the Eq. 6.3 the temperature was calculated to be 460 K. The difference in these two temperatures resulted from using bulk bismuth properties for calculating the temperature change of a thin bismuth film.

It is interesting to notice that the fitted linear functions do not intersect the y-axis at y=0. This behavior will be explained later.

The fitting of the linear dependence of the $-ln(\frac{I}{I_0})$ on the d_{hkl}^{-2} was done for every time point, and the temperature of the bismuth sample was calculated. The temporal evolution of the temperature of the sample after optical excitation for two pump beam fluences is shown in the Fig. 6.7.

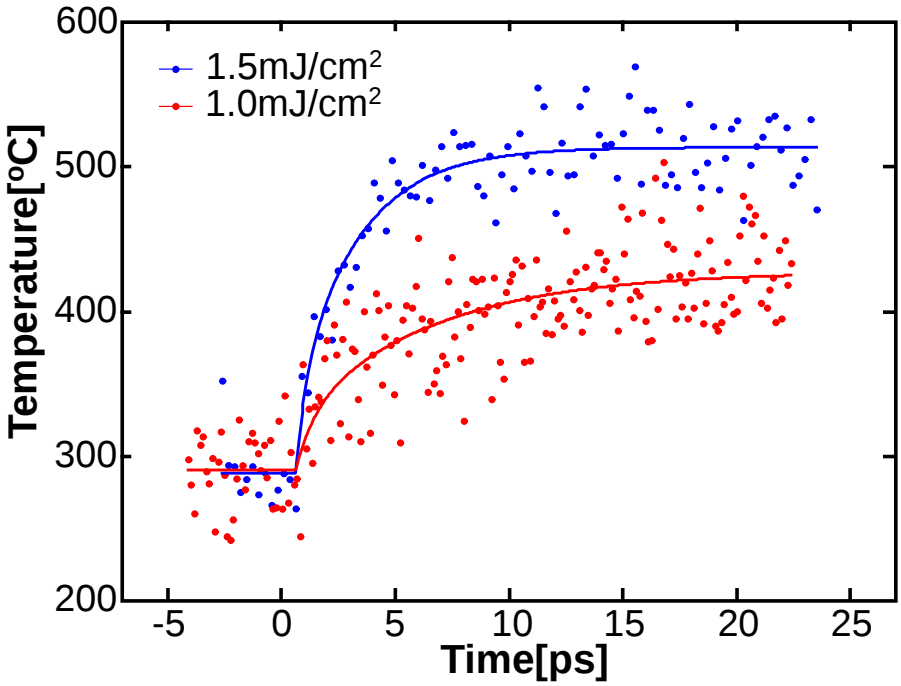

Figure 6.7: Temporal evolution of the temperature of the sample after the optical excitation for two pump beam fluences.

The temporal change of the lattice temperature can be fitted by two expo-

nential rise functions, with the time constants equivalent to time constants in the fitting function for the intensity drop.

6.1.1 Non-diffracted beam

To solve the problems of the fluctuations in the number of electrons per pulse, we tried to normalize the intensity of the diffracted beams to the intensity of the non-diffracted beam. A non-diffracted beam can also be regarded as the (000) diffraction, where the momentum transfer is equal to zero, thus d_{000} is infinity. The Debye-Waller effect does not predict any change for the intensity of the non-diffracted beam due to the lattice heating, so it should remain constant regardless of the time delay between the pump and the probe beam. However, the experimental results show a different behavior (Fig 6.8).

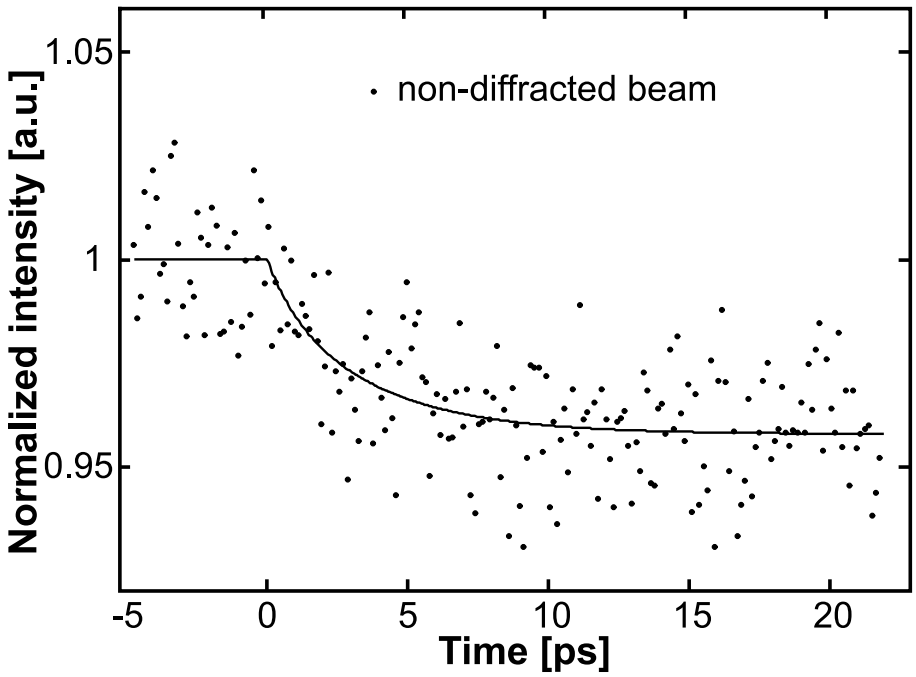

Figure 6.8: The intensity drop of the non-diffracted beam.

At time zero, the intensity of the non-diffracted beam decreased by 4.5%, and the time constant for this drop was 3 ps. However, it is not completely clear if this drop also consisted of two drops, as observed in the case of the diffracted spots. The reason for the change of the intensity of the non-diffracted beam is not yet understood. One of the possible answers is that the inelastic scattering increases with the temperature of the sample, thus decreasing the intensity of the non-diffracted beam.

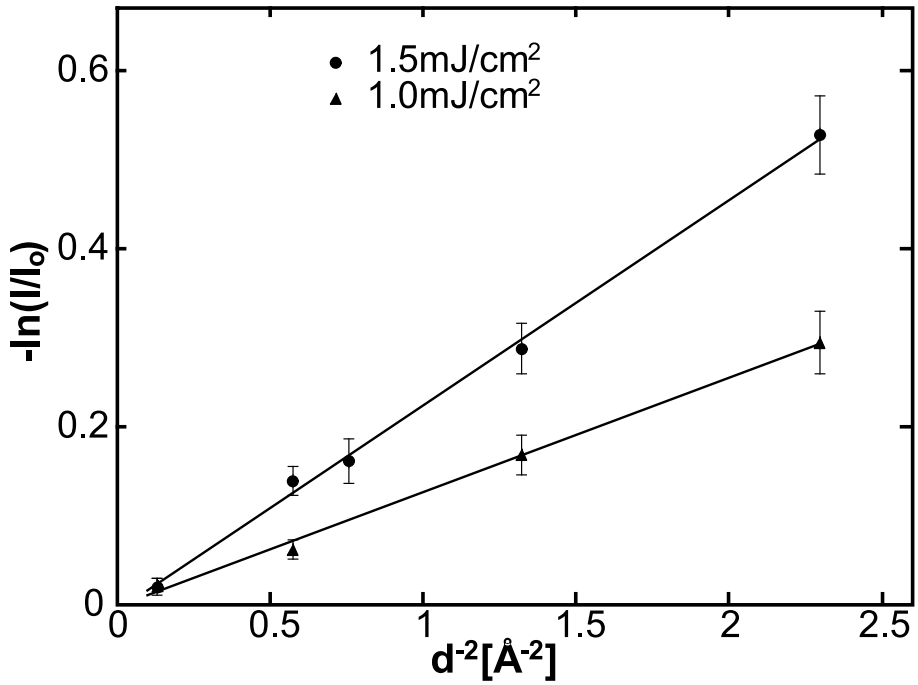

Figure 6.9: Debye-Waller factor value for different fluences and different diffraction orders, normalized to the non-diffracted beam.

The assumption can be made that not only the non-diffracted, but also all of the diffracted beams have the same decrease of intensity. In order to observe only the changes in the diffracted beam induced by the Debye-Waller effect, the final drop of the diffracted beams should be normalized to the final intensity

of the non-diffracted beam. The graph showing the Debye-Waller factor of the diffracted beams normalized to the non-diffracted beam for two different pump fluences is shown in Fig. 6.9

In this case the linear fit passes through zero, as the Debye-Waller theory predicts. This could imply that all the electrons passing through the sample, both the non-diffracted and the diffracted ones, were equally influenced by the same effect which lowered each beam intensity by the same factor.

Chapter 7

Summary and conclusion

This thesis contains work on the design and the realization of an experimental setup capable of providing sub-picosecond electron pulses for ultrafast electron diffraction experiments, and performing the study of ultrafast dynamics in bismuth after optical excitation using this setup.

The aim was to generate electron pulses with sub-picosecond duration and to understand how electron pulses temporally broaden while traveling from the photocathode to the sample. The electron pulse dynamics were simulated and the outcome was an optimized electron source which could achieve sub-picosecond resolution if the number of electrons per pulse was kept low, up to a few thousand.

The diameter, duration, stability and number of electrons per pulse of electron pulses were characterized. The focusing properties of both the electrostatic and magnetic lenses were compared. It was found that focused electron pulses had a diameter of 200 μm at the sample and 450 μm at the detector screen. A pulse duration of 700 fs was estimated for the electron pulses containing 3000

electrons. The stability of the electron source current was sufficient for performing time resolved experiments over long time, on the time scale of several hours.

Time resolved ultrafast electron diffraction experiments were performed on thin bismuth films.
Intensity drops of diffraction spots were observed for different diffraction orders. This intensity drops can be well explained by the Debye-Waller effect and can be used for determining the transient lattice heating.

The time evolution of the diffracted intensity showed that there were two processes responsible for drops. One of them was found to have a characteristic time of 700 fs, while the other was slower and had a characteristic time of 6 ps. The reason for this kind of behavior is not known and has not been reported experimentally for bismuth

The non-diffracted beam showed another interesting behavior. Although the theory for the Debye-Waller effect does not predict any change of intensity, the non-diffracted beam also demonstrates an intensity drop after the sample excitation.

The results have shown that this electron diffraction setup is capable of performing experiments where the information obtained from the intensity of the diffracted beams can provide important data about the structural changes in the crystal lattice.

The experiments discovered new, unexpected behavior which require further experiments in order to be properly understood. It would be of great interest to know how semimetals behave after optical excitation and the reason for the intensity change of the non-diffracted beam.

In these experiments it was possible to observe the thermal lattice responce to the optical excitation. However, because of the orientation of the bismuth crystal, it was not possible to see diffraction spots with Miller index $l \neq 0$ which carry information about the inner cell dynamics. As a result, the intensity change coming from the optical phonon A_{1g} [Ref. 65] could not be seen. By rotating the sample, it is possible to see spots with $l \neq 0$. The static electron diffraction images of rotated sample confirm this.

The observation of the optical phonon can be another means for determining the temporal resolution of the experimental setup. So far, the time resolution was experimentally estimated from the intensity drops of the diffracted spots. The optical phonon is, as reported, much faster than other processes that occur in bismuth lattice after optical excitation. Thus the observation of the optical phonon would be appropriate measurement for determining the temporal resolution.

Appendix A

Leapfrog integration

This is the short introduction to the leapfrog integration method [Ref. 78].

In second-order systems, it is often advantageous to define the velocities ($v = \frac{dx}{dt}$) at the mid-points of the intervals. If a velocity is defined as:

$$v_{i+\frac{1}{2}} = v(t + \frac{\delta t}{2}), \quad i = 0, 1, 2... \tag{A.1}$$

then the change of the position and the velocity are calculated as:

$$x_{i+1} = x_i + v_{i+\frac{1}{2}} \cdot \delta t \tag{A.2a}$$

$$v_{i+\frac{3}{2}} = v_{i+\frac{1}{2}} + a_i \cdot \delta t \tag{A.2b}$$

The schematic represantation of the leapfrog method can be seen in Fig. A.1

Eq. A.2 can be rewritten using only integer indices:

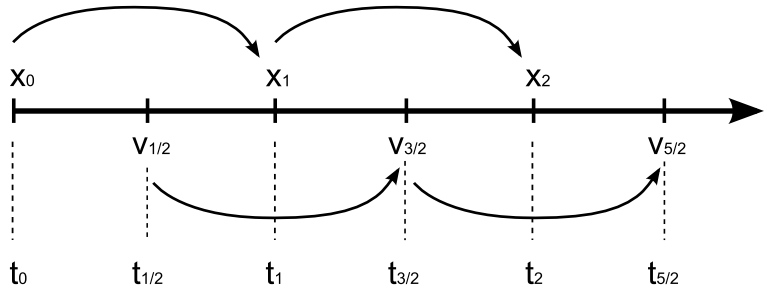

Figure A.1: Schematic representation of the leapfrog method

$$x_{i+1} = x_i + v_i \cdot \delta t + a_i \frac{\delta t^2}{2} \tag{A.3a}$$

$$v_{i+1} = v_i + (a_i + a_{i+1}) \frac{\delta t}{2} \tag{A.3b}$$

The Matlab code for leapfrog integration that I used for calculating the temporal broadening of the electron pulses relies on these two equations.

A.1 Matlab code for leapfrog integration

```
clear
% number of electrons
N=[50,100,200,500,750,1000,1500,2000,5000,10000]

%time step - dt (in ps)
dt=0.3;
% number of steps
M=40000;
% constant (K=e^2/(m_e*epsilon_0*PI) in mm^3/ps^2)
K=1.013e-12;

% duration of electron pulse after acceleration - tt (in ps)
```

```
tt=0.300;
% speed of electrons - ve (30kV, in mm/ps)
ve=0.1;
% length of electron pulse after acceleration - l0 (in mm)
l0=ve*tt;
% radius of electron beam after acceleration(in mm) - r0
r0=0.125;
%first time derivative of length after acceleration
dl0=0;

for p = 1:10

  clear ddl0 l dl ddl x name

  %second time derivative of length
  %after acceleration ddl0 (in mm/s^2)
  ddl0=N(p)*K*(1-(l0/sqrt(l0^2+4*r0^2)))/(r0^2);

  for i = 1:M
     l(i)=0;
     dl(i)=0;
     ddl(i)=0;

    % radius of the pulse changes,
    % angle of divergence is .25 degrees
     r(i)=r0; %+sind(.25)*i*dt*ve;
    %distance that pulse had traveled in i steps
     x(i)=i*dt*ve;
   end

  l(1)=l0+dl0*dt+ddl0*(dt^2)/2;
  ddl(1)=N(p)*K*(1-(l(1)/sqrt((l(1)^2+4*r(1)^2))))/(r(1)^2);
  dl(1)=dl0+(ddl0+ddl(1))*dt/2;
```

```
  G(1,1)=x(1);
  G(1,2)=l(1)/ve;

  for i = 2:M
    l(i)=l(i-1)+dl(i-1)*dt+ddl(i-1)*dt^2/2;
    ddl(i)=N(p)*K*(1-(l(i)/sqrt((l(i)^2+4*r(i)^2))))/(r(i)^2);
    dl(i)=dl(i-1)+(ddl(i-1)+ddl(i))*dt/2;
    G(i,1)=x(i);
    G(i,2)=l(i)/ve;
  end

  suffix = int2str(N(p));
  name = ['data_', suffix, '.txt'];
  dlmwrite(name,G,' ');

end
```

Appendix B

Bismuth properties

Bismuth is a semimetal with the A7 or α-arsenic crystal structure which is a rhombohedraly distorted face-centered cubic (fcc) lattice [Ref. 79]. The primitive crystal basis of the lattice consists of two Bismuth atoms separated by a distance which is a little bit less than the half of the body diagonal d ($x_d = 0.486d$).

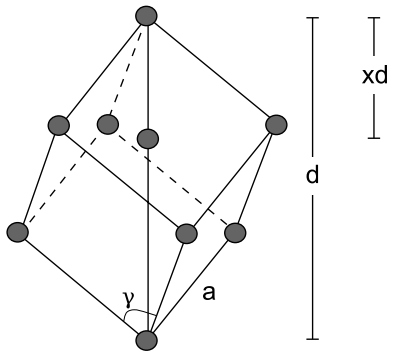

Figure B.1: Bismuth unit cell

The distortion from the cubic structure to A7 is stabilized by the so-called Peierls-Jones mechanism [Ref. 80]. External influences (pressure, temperature,

optical excitation of electrons) can change the equilibrium distance between two basis atoms.

Some basic physical propereties of bismuth [Ref. 70, 81–83] are shown in Table. B.1.

Density	9.78g/cm^3
Melting point	544.7 K
Boiling point	1837 K
Specific heat capacity	122 J/(kg $\cdot$ K)
Linear absorption coefficient for 800nm	$6 \cdot 10^5$ cm^{-1}
Absorption depth for 800nm	16.67 nm
Reflection at 800nm	68%
Debye temperature	112 K

Table B.1: Physical properties of bismuth

Bibliography

[1] D. Strickland and G. Mourou. Compression of amplified chirped optical pulses. *Optics Communications*, **55** (1985) 447–449.

[2] D. Strickland and G. Mourou. Compression of amplified chirped optical pulses. *Optics Communications*, **56** (1985) 219–221.

[3] D. Kuhlke, U. Herpers and D. von der Linde. Soft x-ray emission from subpicosecond laser-produced plasmas. *Applied Physics Letters*, **50** (1987) 1785–1787.

[4] M. M. Murnane, H. C. Kapteyn, M. D. Rosen and R. W. Falcone. Ultrafast X-ray Pulses from Laser-Produced Plasmas. *Science*, **251** (1991) 531–536.

[5] C. Rischel et al. Femtosecond time-resolved X-ray diffraction from laser-heated organic films. *Nature*, **390** (1997) 490–492.

[6] A. L. Cavalieri et al. Clocking Femtosecond X Rays. *Physical Review Letters*, **94** (2005) 114801–4.

[7] A. M. Lindenberg et al. Atomic-Scale Visualization of Inertial Dynamics. *Science*, **308** (2005) 392–395.

[8] B. J. Siwick, J. R. Dwyer, R. E. Jordan and R. J. D. Miller. Ultrafast electron optics: Propagation dynamics of femtosecond electron packets. *Journal of Applied Physics*, **92** (2002) 1643–1648.

[9] B. J. Siwick, J. R. Dwyer, R. E. Jordan and R. J. D. Miller. An Atomic-Level View of Melting Using Femtosecond Electron Diffraction. *Science*, **302** (2003) 1382.

[10] A. Cavalleri. CHEMISTRY: All at Once. *Science*, **318** (2007) 755–756.

[11] S. Williamson, G. Mourou and J. Li. Time-Resolved Laser-Induced Phase-Transformation In Aluminum. *Physical Review Letters*, **52** (1984) 2364–2367.

[12] J. Cao et al. Femtosecond electron diffraction for direct measurement of ultrafast atomic motions. *Applied Physics Letters*, **83** (2003) 1044–1046.

[13] H. Park et al. Optical Control of Coherent Lattice Motions Probed by Femtosecond Electron Diffraction. *Journal of Physical Chemistry B*, **109** (2005) 13854–13856.

[14] H. Park et al. Direct and real-time probing of both coherent and thermal lattice motions. *Solid State Communications*, **136** (2005) 559–563.

[15] M. Harb et al. Electronically Driven Structure Changes of Si Captured by Femtosecond Electron Diffraction. *Physical Review Letters*, **100** (2008) 155504.

[16] M. Harb et al. Carrier Relaxation and Lattice Heating Dynamics in Silicon Revealed by Femtosecond Electron Diffraction. *Journal of Physical Chemistry B*, **110** (2006) 25308–25313.

[17] J. Feenstra, S. Park and A. Zewail. Excited state molecular structures and reactions directly determined by ultrafast electron diffraction. *Journal Of Chemical Physics*, **123** (2005) 221104.

[18] S. Park, J. Feenstra and A. Zewail. Ultrafast electron diffraction: Excited state structures and chemistries of aromatic carbonyls. *Journal of Chemical Physics*, **124** (2006) 174707.

[19] M. Grinolds, V. Lobastov, J. Weissenrieder and A. Zewail. Four-dimensional ultrafast electron microscopy of phase transitions. *Proceedings of the National Academy of Sciences of the United States of America*, **103** (2006) 18427–18431.

[20] J. C. Polanyi and A. H. Zewail. Direct Observation of the Transition State. *Accounts Chem. Res.*, **28** (1995) 119.

[21] R. Karrer et al. Design of a miniature picosecond low-energy electron gun for time-resolved scattering experiments. *Review of Scientific Instruments*, **72** (2001) 4404–4407.

[22] A. Janzen et al. A pulsed electron gun for ultrafast electron diffraction at surfaces. *Review of Scientific Instruments*, **78** (2007) 013906–7.

[23] B. Krenzer et al. Thermal boundary conductance in heterostructures studied by ultrafast electron diffraction. *New Journal of Physics*, **8** (2006) 190–190.

[24] A. Janzen et al. Ultrafast electron diffraction at surfaces after laser excitation. *Surface Science*, **18** (2006) 4094–4098.

[25] A. Hanisch et al. Thermal response of epitaxial thin Bi films on Si(001) upon femtosecond laser excitation studied by ultrafast electron diffraction. *Physical Review B (Condensed Matter and Materials Physics)*, **77** (2008) 125410–6.

[26] A. K. Sharma et al. Measuring pulse-front tilt in ultrashort pulselaser beams without ambiguity of its sign usingsingle-shot tilted pulse-front autocorrelator. *Opt. Express*, **14** (2006) 13131–13141.

[27] A. K. Sharma et al. Measuring pulse-front tilt in ultrashort pulse laser beams without ambiguity of its sign using single-shot tilted pulse-front autocorrelator: Erratum. *Opt. Express*, **15** (2007) 7537–7537.

[28] P. Baum and A. Zewail. Breaking resolution limits in ultrafast electron diffraction and microscopy. *Proceedings of the National Academy of Sciences of the United States of America*, **103** (2006) 16105–16110.

[29] P. Baum, D.-S. Yang and A. H. Zewail. 4D Visualization of Transitional Structures in Phase Transformations by Electron Diffraction. *Science*, **318** (2007) 788–792.

[30] T. van Oudheusden et al. Electron source concept for single-shot sub-100 fs electron diffraction in the 100 keV range. *Journal of Applied Physics*, **102** (2007) 093501–8.

[31] L. Veisz et al. Hybrid dc–ac electron gun for fs-electron pulse generation. *New Journal of Physics*, **9** (2007) 451–451.

[32] B. J. Siwick. *Femtosecond Electron Diffraction Studies of Strongly-Driven Structural Phase Transitions*. Ph.D. thesis, University of Toronto, 2004.

[33] P. Gallant et al. Characterization of a subpicosecond x-ray streak camera for ultrashort laser-produced plasmas experiments. *Review of Scientific Instruments*, **71** (2000) 3627–3633.

[34] R. Shepherd et al. Ultrafast x-ray streak camera for use in ultrashort laser-produced plasma research. *Review of Scientific Instruments*, **66** (1995) 719–721.

[35] B.-L. Qian and H. E. Elsayed-Ali. Comment on "Ultrafast electron optics: Propagation dynamics of femtosecond electron packets" [J. Appl. Phys. 92, 1643 (2002)]. *Journal of Applied Physics*, **94** (2003) 803–806.

[36] B. J. Siwick, J. R. Dwyer, R. E. Jordan and R. J. D. Miller. Response to "Comment on 'Ultrafast electron optics: Propagation dynamics of femtosecond electron packets' " [J. Appl. Phys. 94, 803 (2003)]. *Journal of Applied Physics*, **94** (2003) 807–808.

[37] B.-L. Qian and H. E. Elsayed-Ali. Electron pulse broadening due to space charge effects in a photoelectron gun for electron diffraction and streak camera systems. *Journal of Applied Physics*, **91** (2002) 462–468.

[38] J. D. Jackson. *Classical electrodynamics* (Wiley, New York, 1975), 2d ed. edition.

[39] P. Grivet. *Electron optics. Part 1: Optics* (Pergamon Press, 1972).

[40] V. E. Cosslett. *Introduction to Electron Optics: The Production, Propagation, and Focusing of Electron Beams* (Oxford, Oxford University Press., 1950).

[41] W. Rogowski. Die elektrische Festigkeit am Rande des Plattenkondensators. *Electrical Engineering (Archiv für Elektrotechnik)*, **12** (1923) 1–15.

[42] W. Rogowski and H. Rengier. Ebene Funkenstrecke mit richtiger Randausbildung. *Electrical Engineering (Archiv für Elektrotechnik)*, **16** (1926) 73–75.

[43] H. Rengier. Die Durchbruchfeldstärke der Luft bei ebenen Elektroden mit richtiger und falscher Randausbildung. *Electrical Engineering (Archiv für Elektrotechnik)*, **16** (1926) 76–96.

[44] T. Tsang, T. Srinivasan-Rao and J. Fischer. Surface-plasmon field-enhanced multiphoton photoelectric emission from metal films. *Physical Review B*, **43** (1991) 8870.

[45] M. Pessot, P. Maine and G. Mourou. 1000 times expansion/compression of optical pulses for chirped pulse amplification. *Optics Communications*, **62** (1987) 419–421.

[46] M. Pessot, J. Squier, G. Mourou and D. J. Harter. Chirped-pulse amplification of 100-fsec pulses. *Opt. Lett.*, **14** (1989) 797.

[47] J. S. Feenstra. *Ultrafast Electron Diffraction: Direct Determination of Structural Dynamics of Molecular Excited States*. Ph.D. thesis, California Institute of Technology, Pasadena, California, 2006.

[48] E. L. Crow and K. Shimizu. *Lognormal distributions: theory and applications*. Statistics, textbooks and monographs ; v. 88 (M. Dekker, New York, 1988).

[49] Product information provided by Burle.

[50] J. L. Wiza. Microchannel Plate Detectors. *Nuclear Instruments and Methods*, **162** (1979) 587–601.

[51] N. W. Ashcroft and N. D. Mermin. *Solid state physics* (Holt, Rinehart and Winston, New York, 1976).

[52] C. Kittel. *Introduction to solid state physics* (Wiley, New York, 1986), 6th ed. edition.

[53] J. M. J. M. Cowley. *Electron diffraction techniques*. International Union of Crystallography monographs on crystallography ; 3-4 (International Union of CrystallographyOxford University Press, Chester, England], 1992).

[54] W. Bragg. The diffraction of short electromagnetic waves by a crystal. *Proc. Camb. Phil. Soc*, **17** (1913) 43–57.

[55] M. T. Dove. *Structure and dynamics: an atomic view of materials*. Oxford master series in condensed matter physics (Oxford University Press, Oxford, 2003).

[56] K. Oura et al. *Surface science: an introduction*. Advanced texts in physics (Springer, Berlin, 2003).

[57] P. Debye. Interferenz von Röntgenstrahlen und Wärmebewegung. *Ann. d. Phys.*, **348** (1914) 49.

[58] I. Waller. Zur Frage der Einwirkung der Wärmebewegung auf die Interferenz von Röntgenstrahlen. *Z Phys.*, **17** (1923) 398.

[59] G. Busch and H. Schade. *Lectures on solid state physics*. International series in natural philosophy ; v. 79 (Pergamon Press, Oxford, 1976).

[60] B. C. Larson, J. Z. Tischler and D. M. Mills. Nanosecond resolution time-resolved x-ray study of silicon during pulsed-laser irradiation. *Journal of Materials Research*, **1** (1986) 144.

[61] H. Park et al. Synchronization of femtosecond laser and electron pulses with subpicosecond precision. *Review of Scientific Instruments*, **76** (2005) 083905–4.

[62] A. Dolocan et al. Electron–Photon Pulse Correlator Based on Space-Charge Effects in a Metal Pinhole. *Japanese Journal of Applied Physics*, **45** (2006) 285–291.

[63] J. Williamson et al. Clocking transient chemical changes by ultrafast electron diffraction. *Nature*, **386** (1997) 159–162.

[64] W. R. Pestman. *Mathematical statistics: an introduction*. De Gruyter textbook (Walter de Gruyter, Berlin, 1998).

[65] D. M. Fritz et al. Ultrafast bond softening in bismuth: mapping a solid's interatomic potential with X-rays. *Science*, **315** (2007) 633–636.

[66] T. K. Cheng et al. Mechanism for displacive excitation of coherent phonons in Sb, Bi, Te, and Ti2O3. *Applied Physics Letters*, **59** (1991) 1923–1925.

[67] T. K. Cheng et al. Impulsive excitation of coherent phonons observed in reflection in bismuth and antimony. *Applied Physics Letters*, **57** (1990) 1004–1006.

[68] M. F. DeCamp, D. A. Reis, P. H. Bucksbaum and R. Merlin. Dynamics and coherent control of high-amplitude optical phonons in bismuth. *Physical Review B*, **64** (2001) 092301.

[69] A. Q. Wu and X. Xu. Coupling of ultrafast laser energy to coherent phonons in bismuth. *Applied Physics Letters*, **90** (2007) 251111–3.

[70] A. Q. Wu and X. Xu. Coherent phonon excitation in bismuth. *Applied Surface Science*, **253** (2007) 6301–6304.

[71] S. L. Johnson et al. Nanoscale Depth-Resolved Coherent Femtosecond Motion in Laser-Excited Bismuth. *Physical Review Letters*, **100** (2008) 155501.

[72] M. C. Downer and C. V. Shank. Ultrafast heating of silicon on sapphire by femtosecond optical pulses. *Physical Review Letters*, **56** (1986) 761.

[73] Y. F. Ogrin, V. N. Lutskii and M. I. Elinson. Observation of Quantum Size Effects in Thin Bismuth Films. *JETP Lett.*, **3** (1966) 71.

[74] C. A. Hoffman et al. Semimetal-to-semiconductor transition in bismuth thin films. *Physical Review B*, **48** (1993) 11431.

[75] H. T. Chu. Comment on "Semimetal-to-semiconductor transition in bismuth thin films". *Physical Review B*, **51** (1995) 5532.

[76] C. A. Hoffman et al. Reply to "Comment on 'Semimetal-to-semiconductor transition in bismuth thin films' ". *Physical Review B*, **51** (1995) 5535.

[77] A. A. Lopez. Electron-Hole Recombination in Bismuth. *Physical Review*, **175** (1968) 823.

[78] P. Hut and J. Makino. *Moving Stars Around* (The Art of Computational Science, 2007).

[79] O. Madelung. Semiconductors: Physics of Non-tetrahedrally Bonded Elements and Binary Compounds I. In *Landolt-Börnstein, New Series, Group III: Crystal and Solid State Physics*, volume 17, Semiconductors, Part a (Springer, Berlin, 1983).

[80] R. E. S. Peierls. *More surprises in theoretical physics*. Princeton series in physics (Princeton University Press, Princeton, N.J, 1991).

[81] M. Hase, M. Kitajima, S.-i. Nakashima and K. Mizoguchi. Dynamics of Coherent Anharmonic Phonons in Bismuth Using High Density Photoexcitation. *Physical Review Letters*, **88** (2002) 067401.

[82] E. Palik. *Handbook of Optical Constants of Solids* (Academic Press, 1985).

[83] P. Fischer, I. Sosnowska and M. Szymanski. Debye-Waller factor and thermal expansion of arsenic, antimony and bismuth. *Journal of Physics C: Solid State Physics*, **11** (1978) 1043–1051.